

Western New England University

Digital Commons @ Western New England University

Master's Theses - College of Engineering

College of Engineering

2020

Analysis of flow generated by piezoelectric actuator driven oscillating beams

Ganesh Sharma

Follow this and additional works at: <https://digitalcommons.law.wne.edu/coetheses>

Recommended Citation

Sharma, Ganesh, "Analysis of flow generated by piezoelectric actuator driven oscillating beams" (2020). *Master's Theses - College of Engineering*. 18.
<https://digitalcommons.law.wne.edu/coetheses/18>

This Thesis is brought to you for free and open access by the College of Engineering at Digital Commons @ Western New England University. It has been accepted for inclusion in Master's Theses - College of Engineering by an authorized administrator of Digital Commons @ Western New England University.

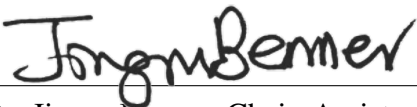

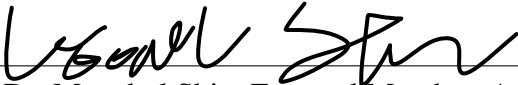

Analysis of Flow Generated by Piezoelectric Actuator Driven Oscillating Beams

Submitted by
Ganesh Sharma

A thesis submitted to the Faculty of
Western New England University
in partial fulfillment of the
requirements for the Master of Science
in Mechanical Engineering

Springfield, MA
Date: August 15, 2020

Approved by

 <hr/>	08/08/2020
Dr. Jingru Benner, Chair, Assistant Professor, ME	Date
 <hr/>	8/8
Dr. Anthony Santamaria, Member, Associate Professor, ME	Date
 <hr/>	8/7/2020
Dr. Moochul Shin, External Member, Associate Professor, CEE	Date
<i>Said Dini</i> <hr/>	08/09/2020
Dr. Said Dini, Department Chair, Professor, ME	Date
 <hr/>	08/10/2020
Dean, College of Engineering	Date

Abstract

Piezoelectric fans are considered a more efficient solution for thermal management purposes with the recent development of small and compact electronics. Traditional axial fans are difficult to scale down and much less efficient when downsized.

Particle Image Velocimetry (PIV) analysis is utilized in this thesis to investigate vortex formation around the trailing edge of a vibrating piezoelectric fan driven at varying power input range from $30V$ to $120V$. The interference between pair of counter-rotating vortices and their impacts on velocity magnitude is also investigated. Vortex formation and detachment is found to occur at an accelerated rate with an increase in Reynold's number. The direction of the vortex pair trajectory is greatly affected by Reynold's number of the flow. The circulation around vortices reaches its maximum quicker with an increase in power input.

IB2d, an immersed boundary method software, is explored for numerical analysis of the flow across the piezoelectric fan. Time-dependent Lagrangian and Eulerian mesh are constructed for each time step using fiber model, allowing immersed boundaries to solve the fully coupled fluid-structure interaction problem. When compared, a vast discrepancy is found between the magnitudes of vortices calculated from experimental PIV and Immersed Boundary numerical simulation results.

Acknowledgments

I want to thank my advisor, Dr. Jingru Benner, for her immense, unending support and guidance throughout this research process. For this learning opportunity, I could not have imagined having a better advisor and a mentor.

I would also like to express my gratitude to Navid Ebrahimi and UCLA for carrying out the PIV experiments and for supplying me with the experimental PIV images. It would have been almost impossible for me to perform the experiment at WNE, due to cost and logistical limitations. Furthermore, I would like to thank Rebecca Shannon for assisting me with image processing on PIVLab.

I want to thank the rest of my thesis committee: Dr. Anthony Santamaria, and Dr. Moochul Shin.

Finally, I want to express special thanks to my wife for her unconditional love and support during my career as a graduate student.

Table of Contents

Abstract	i
Acknowledgments	ii
List of Tables	v
List of Figures	vi
Acronyms and Symbols	x
1 Introduction and Objectives	1
2 Background	3
2.1 Piezoelectric Actuators	4
2.1.1 Types of Piezoelectric Actuators	5
2.2 Flow Analysis Across Piezo-fan	6
2.3 Particle Image Velocimetry - Fundamentals	8
2.3.1 PIVlab 2.31 by William Thielicke	9
2.4 Immersed Boundary Method	11
3 Methods and Procedures	12
3.1 PIV Experimental Setup	12
3.2 Resonance Frequency of the Piezoelectric Fan	15
3.3 Amplitude Measurement of the Fan-tip	16
3.4 Reynold's Number	16
3.5 Analyzing images on PIVlab	19

3.5.1	Interrogation Area (IA)	19
3.5.2	Vorticity and Circulation of the Flow Field	20
3.6	Immersed Boundary Method (IBM) Framework	20
3.7	Lagrangian Mesh of the Vibrating Fan	21
3.8	Eulerian Mesh of the Fluid in Control Volume	24
4	Results and Discussion	27
4.1	Vibration of the Fan	27
4.2	Vortex Formation	28
4.3	Circulation and Decay of Vortices	29
4.3.1	Vortex interactions	32
4.3.2	Vortex decaying	33
4.4	Uncertainty Analysis	37
4.5	Immersed Boundary Methods	37
5	Conclusions and Recommendations	45
	Bibliography	47
A	Vorticity Plots for all Voltages	49
B	Velocity Magnitude Plots for all Voltages	52
C	IB2d Manual	55
C.1	Calculation of Leading and Trailing Edge Positions	55
C.2	Target Points	60

List of Tables

1	Material spec of the carbon cloth wing. Source: Matweb	15
2	Attributes of the piezofan corresponding to voltage inputs and Reynold's Numbers	18
3	Coefficient for the best fit sinusoidal curve of the trailing edge's tip.	28
4	Occurrence of fully developed vortex formation and detachment.	28
5	Frame numbers for normalized time for leading edge.	55
6	Pixel location of the leading edge of the fan.	55
7	Coefficients of sinusoidal model for trailing edge of the piezofan.	58
8	Coefficients of sinusoidal model for leading edge of the piezofan.	58

List of Figures

1.1	A typical configuration of a piezoelectric fan in operation [1].	1
2.1	The growth rate of electricity consumption from 2000 to 2010. [2] [3]	3
2.2	Distribution of power consumption in data centers [4].	4
2.3	Diagram of a cantilevered rectangular unimorph actuator. Image courtesy of Sitti et al. [5].	5
2.4	Diagram of a cantilevered rectangular bimorph actuator.	6
2.5	A classic 2D PIV setup. Image courtesy of Borgoltz (Virginia Tech.).[6]	9
2.6	Processed image with CLAHE and intensity capping. Each square represents a seeding particle for analysis.	10
3.1	Schematic of the PIV experimental setup.	12
3.2	Bimitech <i>EagleTM</i> piezoelectric actuator and fan configuration. Geometric dimensions are given in <i>mm</i>	13
3.3	2-D cross section of Bimitech actuator-fan assembly. Note: figure is not drawn to scale.	14
3.4	Calibration image for the experiment. 1 pixel = 0.018363 mm.	16
3.5	Stacked image of one complete cycle for amplitude measurement.	17
3.6	Comparison of displacement vector densities for different interrogation areas.	19
3.7	A brief guide to the basic steps in Peskin’s immersed boundary method.	22
3.8	Two Lagrangian points connected by spring with zero resting length. F_{spring} is a result of the change in displacement on spring, d . Image courtesy of Battista [7].	23
3.9	Zoomed in time-step illustration of immersed boundary of the fan.	23
3.10	Mesh of the immersed boundary with 512×512 Eulerian grids.	25

3.11	Zoomed in view of the IB mesh.	26
4.1	Fan-tip position of the trailing edge.	27
4.2	Time sequence of vortex ($1/s$) formation and evolution in the propagating regime at $Re = 72.4$	29
4.3	Vortex path from $t = 0T$ to $t = 7T/8$ for $Re = 72.4$	30
4.4	Time sequence of vortex ($1/s$) formation and evolution in the propagating regime at $Re = 281.8$	30
4.5	Vortex trajectory for 115V at 50Hz for one complete oscillation. $Re = 281.8$.	31
4.6	Circulation of counter-rotating vortices at $t = T/8$. Power input = 30.0V	31
4.7	Velocity magnitude for power input of 30V at 50Hz. Velocity profile across the overlapping region of counter-rotating vortices is plotted on Figure 4.8.	32
4.8	Velocity magnitude profile across the overlapping region.	33
4.9	Instantaneous velocity components of two counter-rotating Lamb-Oseen vortices.	34
4.10	Tangential velocity profile of a CCW-rotating vortex. Refer to Figure 4.6a on how 30 concentric circles are drawn around a vortex.	35
4.11	Normalized circulation around CW vortex in one cycle of oscillation as function of unitless t/T	36
4.12	Pressure across the immersed boundary at time step = 2 ($t = 2 \times 10^{-7}$ seconds.)	38
4.13	Pressure across the immersed boundary at $t = 99 \times 10^{-7}$ seconds.	39
4.14	Pressure across the immersed boundary at $t = 369 \times 10^{-7}$ seconds.	40
4.15	Vortices across the immersed boundary at time step = 2 ($t = 2 \times 10^{-7}$ seconds.)	42
4.16	Vortices across the immersed boundary at $t = 99 \times 10^{-7}$ seconds.	43
4.17	Vortices across the immersed boundary at $t = 369 \times 10^{-7}$ seconds.	44
A.1	Time sequence of vortex ($1/s$) formation and evolution in the propagating regime at $Re = 72.4$. Power input = 30V 50Hz.	49

A.2	Time sequence of vortex ($1/s$) formation and evolution in the propagating regime at $Re = 131.8$. Power input = 50V 50Hz.	49
A.3	Time sequence of vortex ($1/s$) formation and evolution in the propagating regime at $Re = 177.2$. Power input = 70V 50Hz.	50
A.4	Time sequence of vortex ($1/s$) formation and evolution in the propagating regime at $Re = 249.1$. Power input = 100V 50Hz.	50
A.5	Time sequence of vortex ($1/s$) formation and evolution in the propagating regime at $Re = 256.9$. Power input = 105V 50Hz.	51
A.6	Time sequence of vortex ($1/s$) formation and evolution in the propagating regime at $Re = 289.9$. Power input = 120V 50Hz.	51
B.1	Time sequence of velocity magnitude evolution in the propagating regime at $Re = 72.4$. Power input = 30V 50Hz.	52
B.2	Time sequence of velocity magnitude evolution in the propagating regime at $Re = 131.8$. Power input = 50V 50Hz	52
B.3	Time sequence of velocity magnitude evolution in the propagating regime at $Re = 177.2$. Power input = 70V 50Hz.	53
B.4	Time sequence of velocity magnitude formation in the propagating regime at $Re = 249.1$. Power input = 100V 50Hz	53
B.5	Time sequence of velocity magnitude evolution in the propagating regime at $Re = 256.9$. Power input = 105V 50Hz.	54
B.6	Time sequence of velocity magnitude evolution in the propagating regime at $Re = 289.9$. Power input = 120V 50Hz.	54
C.1	Measurements of pixel location of the trailing edge. The pixel location measurement is approximated using MATLAB <code>imtool</code>	56
C.2	Amplitude versus time of the leading edge of the fan.	57

C.3	Snapshot of <code>input2d</code> file. <code>mu</code> , the dynamic viscosity of air on line 9 is calculated to achieve the Reynold's number on experimental data. <code>Re</code> is calculated with Equation 5.	60
C.4	Snapshot of <code>input2d</code> file. Toggling <code>save_PARM</code> saves and unsaves the signal to <code>.vtk</code> format.	61
C.5	Snapshot of <code>Piezo_Fan_Vertex.m</code> code.	62
C.6	Snapshot of <code>Piezo_Fan_Vertex.m</code> code.	63
C.7	Snapshot of <code>update_Target_Point_Positions.m</code> code.	64

Acronyms and Symbols

Acronym and Symbols	Explanation	Unit
A	Amplitude	[m]
C	Correlation Matrix	[-]
CFD	Computational Fluid Dynamics	[-]
CLAHE	Contrast Limited Adaptive Histogram Equalization	[-]
D	Thickness of the Beam	[m]
DFT	Discrete Fourier Transform	[-]
DPIV	Digital Particle Image Velocimetry	[-]
E	Elastic Modulus	[Pa]
FFT	Fast Fourier Transform	[-]
FSI	Fluid Structure Interaction	[-]
GUI	Graphical User Interface	[-]
I	Moment of Inertia	[kg · m/s ²]
IA	Integration Area	[-]
IBC	Immersed Boundary Condition	[-]
IBM	Immersed Boundary Method	[-]
IT	Information Technology	[-]
L	Length of the fan	[m]
PIV	Particle Image Velocimetry	[-]
PVF	Polyvinyl Fluoride	[-]
PZT	Lead Zirconate Titrate	[-]
Re	Reynold's Number	[-]
ROI	Region of Interest	[-]
UCLA	University of California - Los Angeles	[-]
λ	Natural Frequency	[s ⁻¹]
ω	Vorticity	[s ⁻¹]
ρ	Density	[kg · m/s ²]
ν	Kinematic Viscosity	[m ² /s]
Γ	Circulation	[m ² /s]

1 Introduction and Objectives

With the development of small and compact electronics, piezoelectric fans are considered as a more efficient possible solution for thermal management purposes. A typical piezoelectric fan consists of a PZT (Lead Zirconate Titanate) layers attached to a flexible polymer blade. When voltage is applied on opposite polar ends of the PZT surfaces, one layer contracts while the other expands, creating a bending moment, which ultimately leads to deflection of the actuator in harmonic behavior. Their small size, low power consumption, and low noise generation make them the best alternative for electronic devices [8]. Fluid flow across the piezoelectric blade is induced by converting electrical energy into mechanical vibrations. These fans consume significantly low power compared to axial fans, typically between 1-40 mW and remain relatively noiseless if the operational frequency is kept below 100 Hz (near the hearing threshold of human hearing. When compared to the traditional rotary fan, piezo-fans also has the advantage of no moving parts. These features translate to longer life, better reliability, and much lower maintenance cost [9].

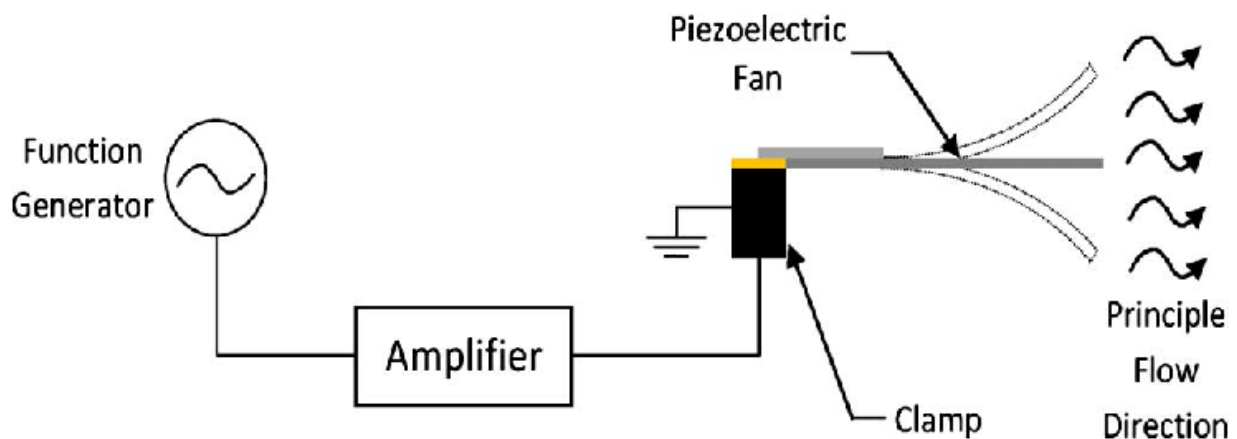


Figure 1.1: A typical configuration of a piezoelectric fan in operation [1].

In this thesis research, flow fields across vibrating piezoelectric blades are analyzed at different power inputs. PIV analysis is performed on sequential images of the flow field across vibrating piezofan. Immersed boundary method is also explored to solve the fluid-structure interaction between the piezofan and the fluid. Vortex evolution and interference between counter-rotating vortices (generated at tips of the fan) is also investigated. Findings from this research on flow properties can be utilized to optimize the device so maximum flow efficiency is achieved.

2 Background

As mankind approached the information age, there has been a significant increase in electricity consumption in IT sector. Taking the worldwide data on energy consumption from 2000 to 2010, the world saw an increase from 71 billion kWh per year to 238 billion kWh per year [2] [3]. Compared to the overall electricity consumption (labeled Δ in Figure 2.1) which averaged approximately 3.0% per year, consumption of data centers (labeled by symbol \square in Figure 2.1) grew at an average of 11% per year. In simple terms, IT equipment have made a great contri-

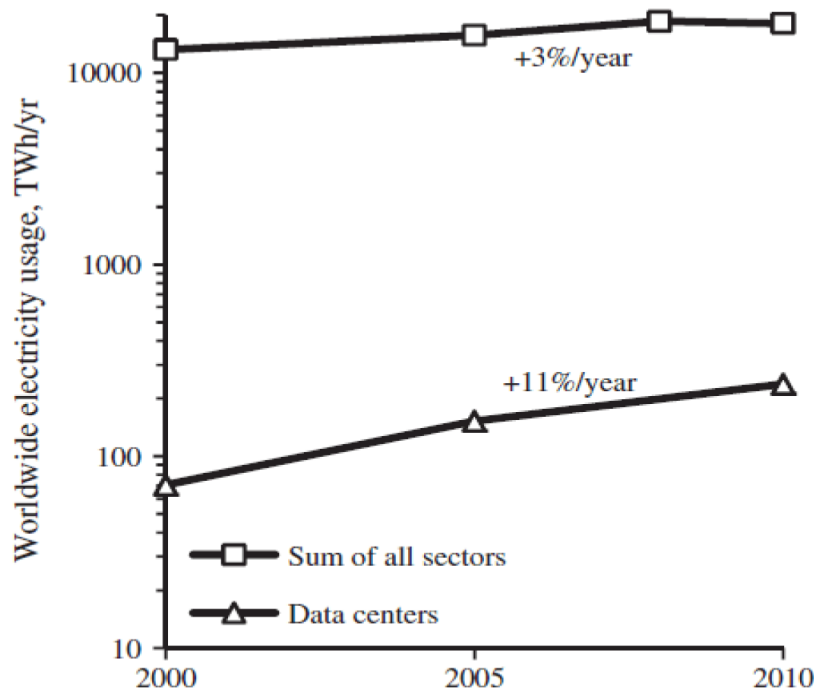


Figure 2.1: The growth rate of electricity consumption from 2000 to 2010. [2] [3]

bution to the global energy use and such staggering growth in electricity usage is expected to increase in the future. Approximately 30% of the electricity is spent on thermal management

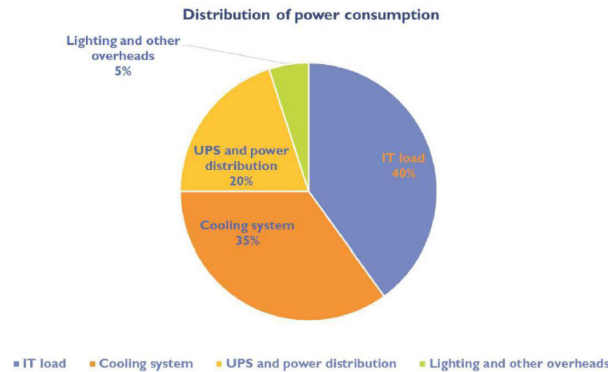


Figure 2.2: Distribution of power consumption in data centers [4].

and cooling systems on data centers. On the other hand, the load itself only consumes 40% of the total power as shown in Figure 2.2 [10]. Although the energy consumption in thermal management has been a rising concern, there exists no effective approach to deal with the thermodynamic problem of the cooling system in these devices [4]. Piezoelectric fans can be used to replace traditional axial fans for thermal management purposes in compact electronics at data centers.

2.1 Piezoelectric Actuators

The piezoelectric effect was discovered in 1880 by two French physicists, Paul and Jacques Curie when the two brothers were experimenting in crystals of quartz, tourmaline and Rochelle salt (scientifically known as Potassium Sodium Tartrate) [11]. The word "Piezoelectric" is derived from the Greek root "*piezein*" which translates to squeeze or press [12]. Similar to magnetic induction, piezoelectric effect is a reversible process, i.e., applied AC input causes bending moment within the piezoelectric material and vice versa.

For material to exhibit piezoelectric effects, the crystalline structure must have no center of symmetry. The material can be a large singular crystals either formed naturally or by synthetic processes. Some of the most common piezoelectric materials used on piezoelectric actuators are

Lead Zirconate Titanate (PZT), and Polymer Polyvinledene Fluoride (PVF) [10].

2.1.1 Types of Piezoelectric Actuators

There are two main types of piezoelectric actuators used throughout the industry [13].

1. **Unimorph** actuator consists of a composite beam formed by attaching active piezoelectric layer to a purely elastic layer. Steel, titanium or composite polymers are usually chosen for the elastic layer. Since unimorph actuators only contain only one active layer, they are

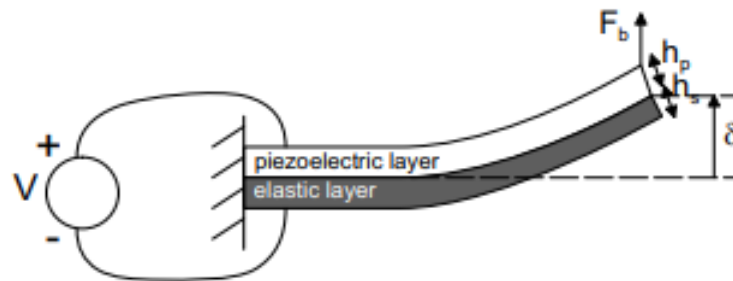


Figure 2.3: Diagram of a cantilevered rectangular unimorph actuator. Image courtesy of Sitti et al. [5].

best suited for lower power consumption environment and highly compact design requirements.

2. **Bimorph** actuators on the other hand contain two layers of active PZT material enveloped to a purely elastic layer. Bimorph actuators can achieve higher amplitude (δ) due to the fact that they contain two layers of active PZT material. Depending on the design needs, combinations of multiple layers of PZT and pure elastic layer may be joined together to acquire the desired stiffness and vibrations. The relationship between amplitude and power inputs are defined in Section 3.

The idea of transforming piezoelectric effect into controllable motions was implemented by researchers during 1930s. Later, in the year 1978, the first studies on the piezoelectric fan for

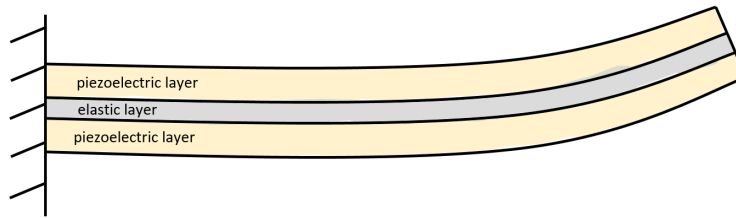


Figure 2.4: Diagram of a cantilevered rectangular bimorph actuator.

thermal management in electronic devices was published by Minoru Toda and Susumu Osaka. Toda and Osaka applied a square wave voltage with an amplitude of $\pm 150\text{V}$ to a stack of four $7\mu\text{m}$ PVF2 plates. The experiment unveiled that piezoelectric fan produced the same amount of airflow as an axial fan but this was accomplished with 678.5% less power input than the axial fan [14].

2.2 Flow Analysis Across Piezo-fan

Flow fields across vibrating piezo-fan have been studied by [15], [16], [17], [18] [19], [20], and [21]. Kim et al. 2004 [20] used phase-resolved particle image velocimetry and smoke visualization techniques to study vortex formation and velocity profiles on vibrating cantilever plates. A pair of counter rotating vortices were formed over each vibration cycle. The two vortices induced a high-velocity region in between them, in which the maximum velocity in the region of interest is nearly four times the maximum speed of the tip of the vibrating plate.

Kimber et al [9] constructed a pressure-flow rate relationship (commonly known as the fan curve) for a piezoelectric fan. In comparison against standard axial fans with comparable weight or stream rate levels, Kimber determined that piezoelectric fans are nearly ten times more efficient in converting input power into useful cooling performance. They also observed that resonance frequency of the piezofan increases with an increase in its stiffness. As expected, an increase in amplitude was observed on softer fans. The maximum heat transfer rate performance

of a given fan is heavily dependent on vibration frequency and oscillation amplitudes. Vibration frequency is found to be more influential than the amplitude [9].

Choi et al. (2012) [19] studied vortex generation around a vibrating cantilever piezofan. The flow studies were performed on experimental and numerical simulations. Numerical simulation was able to reproduce time varying motion of the cantilever beam realistically compared to experimental boundary conditions. Gradients in static pressures at the tip of the beam caused the formation of vortex across the fan. They also ascertained that the trajectory of vortices and their sizes on simulation were smaller than the experimental value. Vortex formation are categorized into four distinct stages: 1. Initiation 2. Development 3. Separation, and 4. Propagation

The investigation by Ebrahimi et al. [15] uncovered that the average mass-flow (\dot{m}) across the control volume around piezoelectric fan is significantly affected by the vortex regime. They categorize the evolution of vortex regimes into three distinct phases based on Reynold's number:

1. **Non-propagating regime** ($Re < 37$): Vortices on this category disappear with the generation of the subsequent vortex .
2. **Intermediate regime** $37 < Re < 70$: Vortices on this regime are weak and detach from the trailing of the blade but dissipate quickly.
3. **Propagating regime** $Re > 70$: Vortices on this category do not dissipate and travel as a pair once subsequent vortex is generated.

They also observed that vortex regimes significantly affect the strength of fluid jet downstream of the vibrating blade.

Bidakhvidi et al. (2013)[22] performed dynamic analysis on varying geometrical shapes of piezoelectric fan. The analyses determined that piezoelectric fans induce optimum flow fields

while operating at its resonance frequency. They also established that the phased-averaged velocity increases with an increasing amplitude of the piezoelectric fan if frequency input is kept constant.

2.3 Particle Image Velocimetry - Fundamentals

Particle Image Velocimetry (also referred as PIV) is a tool used in fluid dynamics to measure instantaneous velocity of moving fluids with high spatial resolution. Tomo-PIV (tomographic particle image velocimetry) was the first of its kind introduced by Elsinga et al [23]. The flow across a vibrating plate is visualized by illuminating a thin chamber of fluid containing reflective and neutrally buoyant tracer particles. A digital image sensor (high-speed camera) is positioned parallel to the illuminated sheet, capturing the movement of the particles (see Figure 2.5). Two images (A and B) of the illuminated plane captured at t and t' are analyzed. For the experimental set up in this research, a high speed camera is used to take sequential frames of the moving fluid. Each frame is then divided into small subsections called Interrogation Area (IA) in which the vector difference between each seeding particles' movements in micron-scale are calculated between time = t and t' .

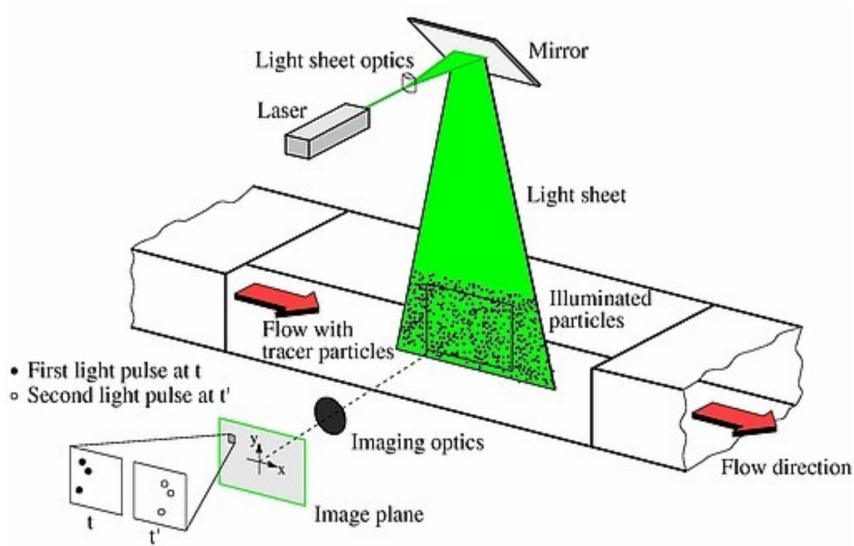


Figure 2.5: A classic 2D PIV setup. Image courtesy of Borgoltz (Virginia Tech.).[6]

The movement of particle-seeded by flow is calculated numerically by Equation 1 where $\Delta t = t' - t$. [24]

$$\vec{V} = \frac{\Delta \vec{X}}{\Delta t} \quad (1)$$

2.3.1 PIVlab 2.31 by William Thielicke

PIVlab is a MATLAB GUI toolbox developed by William Thielicke [25] solely for the purpose of non-intrusive Digital Particle Image Velocimetry (DPIV also referred as PIV). This analysis tool consists of three main functions:

1. **Image Pre-processing:** Sequential frames are enhanced using contrast limited adaptive histogram equalization (CLAHE) and intensity capping. CLAHE adjusts the intensities of images with histograms that are spread-out to full range from 0 to 255 in 8-bit images.[25]
2. **Image Evaluation:** The interrogation area from subsequent images (ie image A and B) are cross correlated to derive the most probable particle displacement. Thielicke [25]

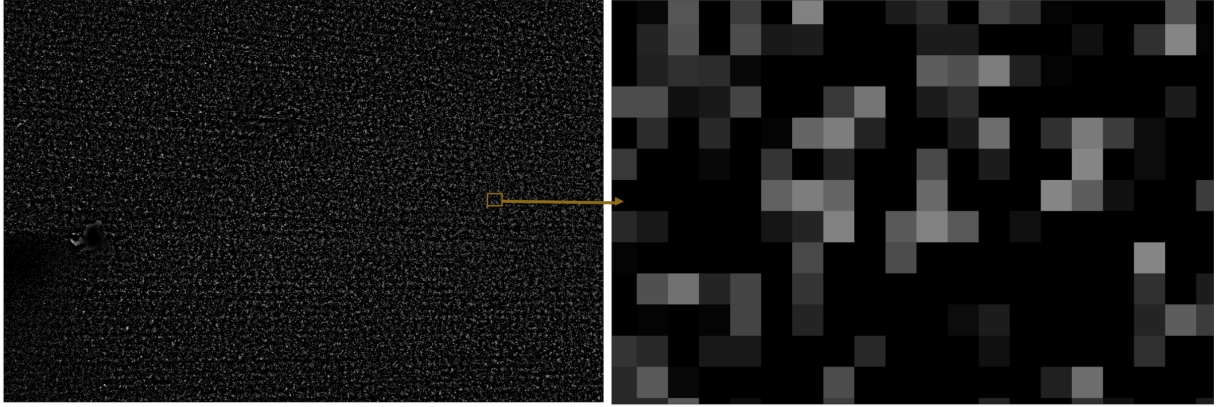


Figure 2.6: Processed image with CLAHE and intensity capping. Each square represents a seeding particle for analysis.

computes the discrete cross-correlation function for a particle in image A and B using Equation 2. The location of the intensity peak in correlation matrix C gives displacement of particles from A to B. [25]

$$C(m, n) = \sum_i \sum_j A(i, j) B(i - m, j - n) \quad (2)$$

In PIVlab, discrete Fourier Transform (DFT) is used to solve for correlation (C) in frequency domain.

3. **Post-processing:** PIVlab contains velocity limits, standard deviation filter and normalized median statistical algorithm to validate the raw-calculated vectors. The software then uses interpolation to compute missing information that were previously omitted by velocity limits and standard deviation. Besides velocity profiles, PIVlab also has the capability to extract vorticity, circulation, and divergence of a given flow field. Displacement vectors calculated by DPIV is never free of noise and missing vector on sections of interrogation area. PIV utilizes "Data Smoothing" functionality to reduce the noise induced by poor lighting or erratic pixels. Data smoothing is accomplished by performing bi-linear

interpolation of vectors within the vicinity of inconsistent vectors.

2.4 Immersed Boundary Method

Immersed Boundary Method (IBM) in CFD is a method first introduced by Charles Peskin in 1972 to simulate Fluid Structure Interaction (FSI) of blood flow around valve leaflets of the heart [7]. Battista developed IB2d, an immersed boundary method solver which solves fluid structure interaction problem by incorporating fiber models into both fluid and immersed boundary. The software computes the force density around the immersed structure for continuous time-steps. The software then solves for deformation of Lagrangian nodes (displacements). FFT is then used to resolve the Navier-Stokes equations to compute fluid velocities within fluid domain [7]. IB2d manual and its full functionality are elaborated on Appendix C.

3 Methods and Procedures

3.1 PIV Experimental Setup

The experimental setup consists of a carbon fiber blade attached to a Bimitech Eagle piezoelectric actuator. The actuator is clamped to a stand (see Figure 3.1). AMETEK Phantom camera body with $f/2$ lens is used to take high-speed picture of vibrating piezoelectric fan at 8800 frames-per-second. Due to the logistics and cost related issues, the experimental setup and data collection were conducted in collaboration with Ebrahimi [15] at University of California Los Angeles (UCLA).

Supporting hinges are clamped firmly to avoid any unnecessary movement of the Bimitech fan during its operation. For this experiment, power input ranging from 30V to 120V at constant

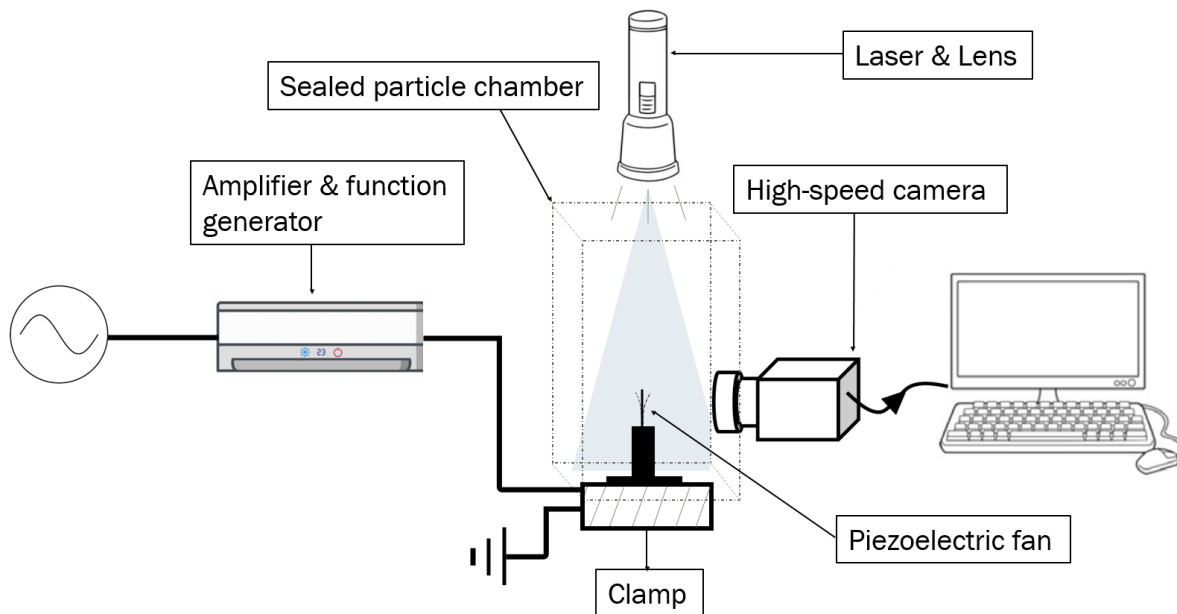


Figure 3.1: Schematic of the PIV experimental setup.

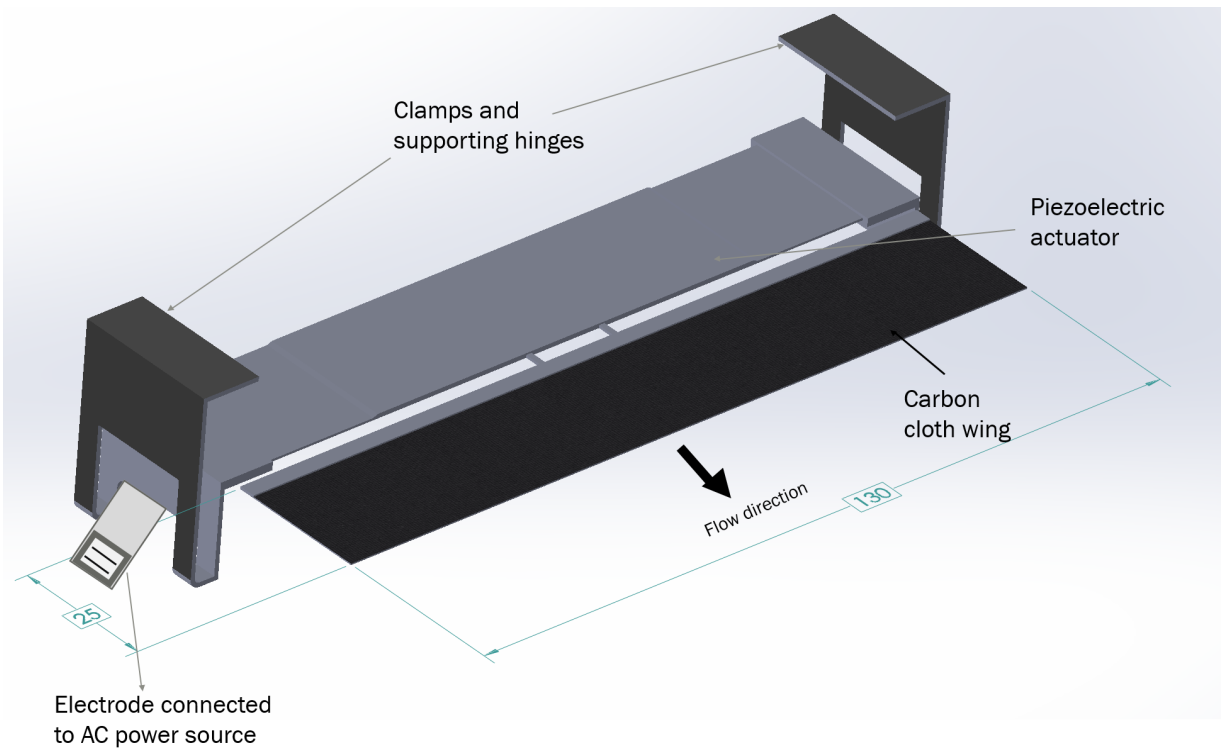


Figure 3.2: Bimitech *Eagle*TM piezoelectric actuator and fan configuration. Geometric dimensions are given in *mm*.

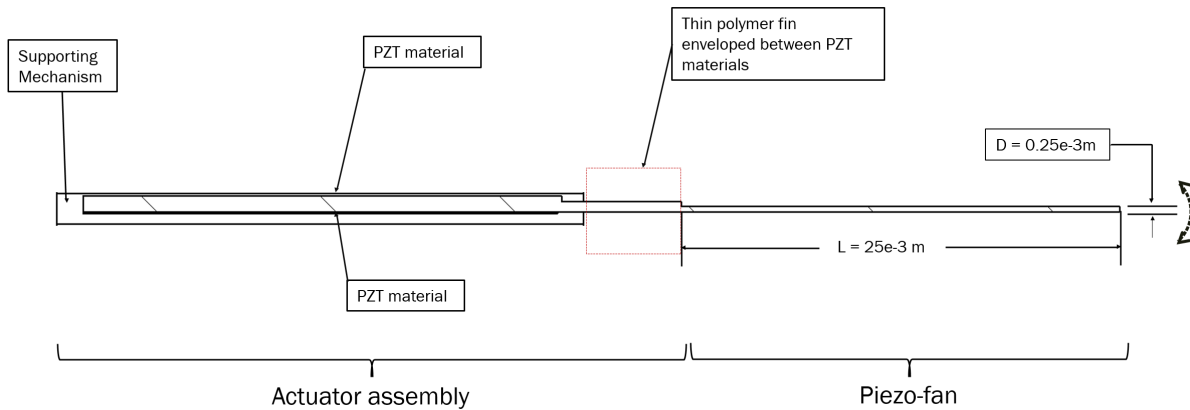


Figure 3.3: 2-D cross section of Bimitech actuator-fan assembly. Note: figure is not drawn to scale.

frequency of 50Hz is applied to the piezoelectric actuator. These voltages are achieved by amplifying sinusoidal voltage waves of amplitude 0.05V to 2.0V from a function generator (Model 33220A, Agilent). Variations in voltage while keeping the frequency constant will help understand the direct effect of voltages on flow field properties.

PIV setup in this experiment incorporates a 500 mW continuous wave laser (Model PZD700A, TREK) with a wavelength of 532 nm . The laser beam is shaped into light sheet using cylindrical lens (plano-concave lens, $f = -3.9\text{ mm}$, Thorlabs). High speed camera (Phantom VEO-640L) is employed to capture the motion of particle in region of interest (ROI). The camera is equipped to take 15-bit of grayscale frames with the resolution of 4-megapixel. The frame speed is set to 8800 fps (shutter speed = 1.136 ms). Setting the frame speed to this incredibly high range will assist in capturing at-least 100 frames for one complete oscillation of the piezo-fan, even for higher power inputs. The experiments are conducted in a sealed box made of transparent acrylic plates measuring $30\text{ cm} \times 20\text{ cm} \times 8\text{ cm}$. Sealed box of this dimension is large enough to reduce interference from the side walls. The seeding particles are generated by heating a solution of water and glycerin ($30\% \text{ v/v}$ ratio). Before performing subsequent experiments, the

Table 1: Material spec of the carbon cloth wing. Source: Matweb

Material Spec	Values
E	41.0GPa.
L	25.0mm
D	0.25mm
ρ	1.0g/cm ³
mass	0.477g

seeding particles are allowed to rest for a minute to minimize any disturbances [15].

3.2 Resonance Frequency of the Piezoelectric Fan

Piezofans achieve maximum amplitude when the actuator vibrates at its natural frequency. Using Chen [26]'s method, Equation 3, the natural frequency of the piezoelectric fan is approximately 57 Hz. To account for dampening effects due to air molecules disturbances from the enclosed wall surface, frequency slightly lower than the natural frequency of 50Hz is used to obtain maximum fan performance.

$$\lambda_n = \sqrt{\frac{F_{cr}}{EI}} \quad (3)$$

$$F_{cr} = EI \frac{\pi^2}{4L^2} \quad (4)$$

Then using the values from Table 1:

$$I = \frac{1}{12}LD^3$$

$$\lambda_n = 57Hz.$$

3.3 Amplitude Measurement of the Fan-tip

Co-ordinates for the locations of fan-tip positions are precisely measured on MATLAB. The pixel to standard units conversion is done using a calibration image shown in Figure 3.4. Calibration relationship from Figure 3.4 is used throughout the analysis to calculate flow properties such as velocities, vorticities, and circulation.

All frames from a single oscillation are stacked on MATLAB and the stacked image is conditioned to identify upper and lower range of the fan (see Figure 3.5).

3.4 Reynold's Number

Reynold's Numbers are critical in terms of characterizing vortex regime as discussed previously in Section 2. Higher Reynold's Number is expected for increasing voltage because the

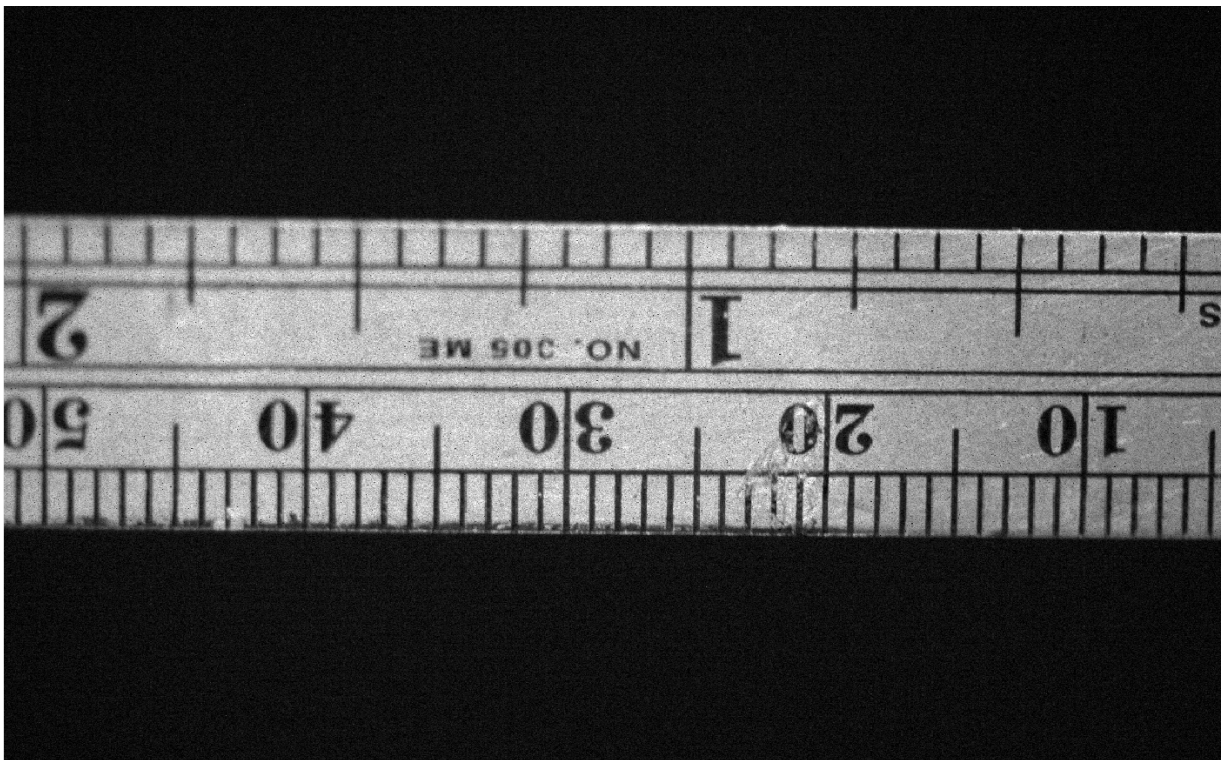


Figure 3.4: Calibration image for the experiment. 1 pixel = 0.018363 mm.

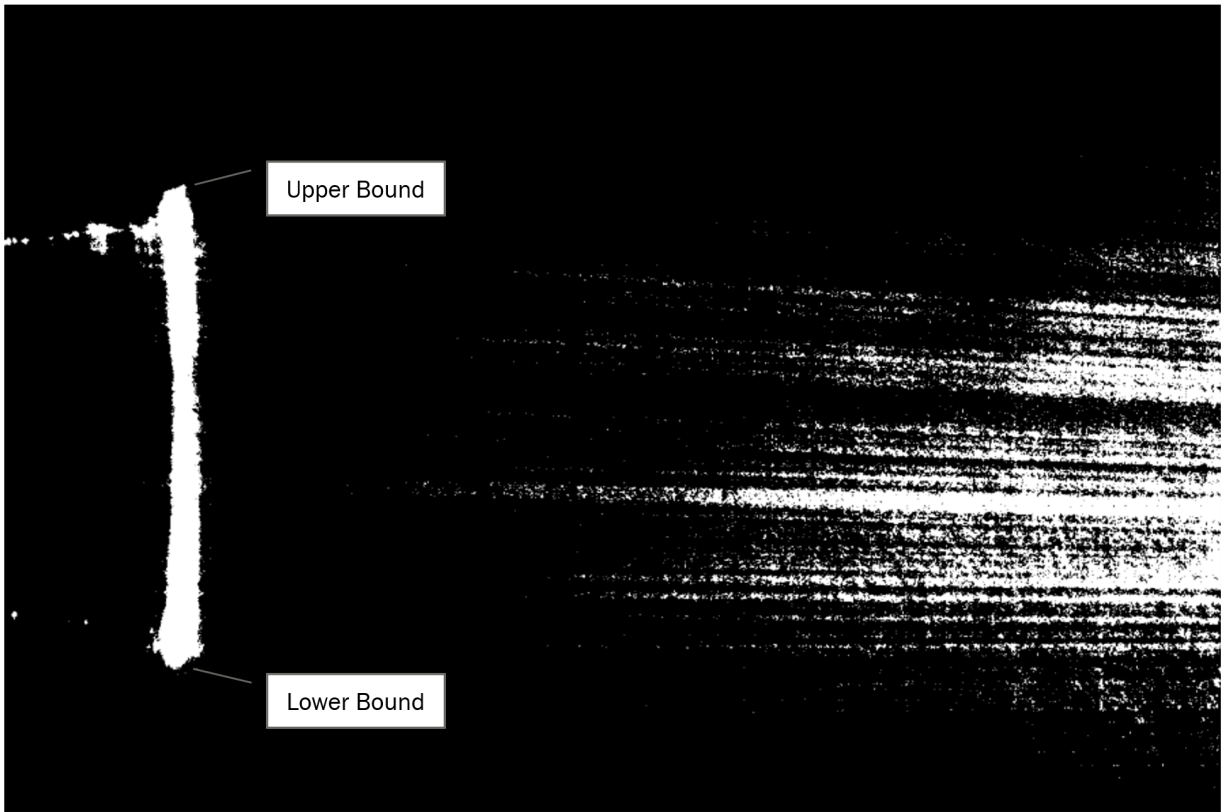


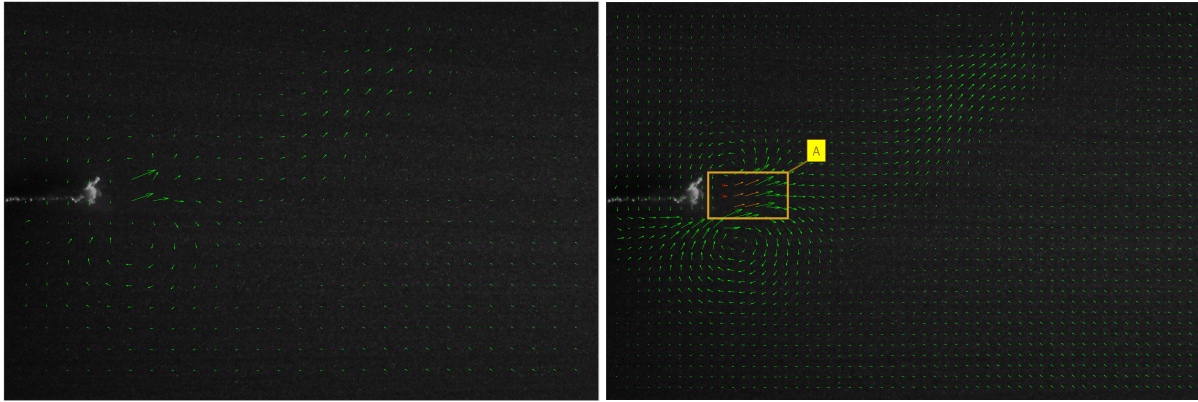
Figure 3.5: Stacked image of one complete cycle for amplitude measurement.

amplitude is expected to increase. To satisfy no-slip condition, velocity of the fan's tip has to be equal to the velocity of fluid across the boundary layer. With this relationship, Reynold's Number is defined based on the maximum tip velocity (U_{tip}) and length of the vibrating beam (L). The maximum tip velocity, u_{tip} , is defined as the product of fan's frequency f and amplitude of the vibration (A). With Ebrahimi's method [15], Reynold's Numbers for each voltages can be calculated with Equation 5 where ν is the kinematic velocity of air.

$$\begin{aligned}
 Re &= \frac{u_{tip}L}{\nu} \\
 &= \frac{fAL}{\nu}
 \end{aligned} \tag{5}$$

Table 2: Attributes of the piezofan corresponding to voltage inputs and Reynold's Numbers

Voltage	$A(m)$	$U_{tip}(m/s)$	Re
30.0V	$0.863e - 3$	0.0431	72.4
50.0V	$1.571e - 3$	0.0786	131.8
70.0V	$2.112e - 3$	0.106	177.2
100.0V	$2.970e - 3$	0.149	249.1
105.0V	$3.063e - 3$	0.153	256.9
115.0V	$3.336e - 3$	0.168	281.8
120.0V	$3.456e - 3$	0.173	289.9



(a) Interrogation window attributes:
 Pass 1 = 120 pixels
 Pass 2 = 64 pixels

(b) Interrogation window attributes:
 Pass 1 = 64 pixels
 Pass 2 = 32 pixels

Figure 3.6: Comparison of displacement vector densities for different interrogation areas.

3.5 Analyzing images on PIVlab

PIVlab 2.31, an open-source Matlab package by Thielicke and Stamhuis [25], is used to analyze experimental images. This software package utilizes Discrete Fourier Transform (DFT) technique in which smaller sub areas (IA) of two successive frames are cross-correlated to obtain direction and magnitude of seeded particle's displacements. The frame speed and the displacement vectors on two subsequent frames are then used to calculate the velocity vectors [15][27].

3.5.1 Interrogation Area (IA)

Choosing the optimal interrogation area is an important task to obtain accurate displacement vectors and to minimize computation time while analyzing numerous images for each voltage. As a rule of thumb, larger IA yields coarser vectors and takes a shorter time to analyze. Conversely, a finer IA, gives much more accurate results but at the cost of an increase in computation time. The larger the interrogation areas, the better the signal-to-noise ratio and the more robust is the cross-correlation. However, large interrogation areas will only give a shallow vector resolution. That is why the interrogation areas for the following passes (pass 2 and pass 3) are reduced.

The displacement information of the first pass is used to offset the interrogation areas in the second pass. This procedure yields a high displacement vector resolution and a high signal-to-noise ratio [28]. Red vectors labeled A in Figure 3.6b are interpolated vectors. Erroneous vectors with unusual direction and magnitude are removed with `Vector Validation` function and are interpolated especially on the poorly illuminated regions [25].

3.5.2 Vorticity and Circulation of the Flow Field

A pair of two counter rotating vortices are generated when fan tip reaches maximum amplitude and returns to origin. Vorticity of the 2D flow field can be calculated with Equation 6, the same method used by [15], [19], and [25].

$$\omega = \frac{\partial v}{\partial x} - \frac{\partial u}{\partial y} \quad (6)$$

Circulation is the line integral along the contour of the component of tangential velocity.

$$\Gamma = \oint \mathbf{U} \cdot d\mathbf{l} \quad (7)$$

Circulation of counter-clockwise vortices are positive whereas clockwise rotating vortices are negative.

3.6 Immersed Boundary Method (IBM) Framework

IB2d framework by Battista [7] is utilized to create experimental boundary conditions of the fan. Battista models the fluid motion using Navier-stokes equation in Eulerian domain.

$$\rho \left(\frac{\partial \mathbf{u}(x, t)}{\partial t} + \mathbf{u}(x, t) \cdot \nabla \mathbf{u}(x, t) \right) = \nabla p(x, t) + \mu \Delta \mathbf{u}(x, t) + \mathbf{f}(x, t) \quad (8)$$

The components of Equation 8 are described below:

- $\mathbf{u}(x, t)$ is the fluid velocity in u-direction
- $\mathbf{v}(x, t)$ is the fluid velocity in v-direction
- $\mathbf{p}(x, t)$ is the pressure acting on fluid
- $\mathbf{f}(x, t)$ is the force per unit volume
- $x = (x, y)$ and $t = \text{time}$

Fluid and immersed structure interaction is given by

$$\mathbf{f}(x, t) = \int \mathbf{F}(r, t) \delta(\mathbf{x} - \mathbf{X}(r, t)) dr \quad (9)$$

$$\begin{aligned} U(X(r, t), t) &= \frac{\partial X(r, t)}{\partial t} \\ &= \int \mathbf{u}(x, t) \delta(x - X(r, t)) dx \end{aligned} \quad (10)$$

where $F(r, t)$ is the force per unit area on the fluid by elastic deformation, $X(r, t)$ is the Cartesian coordinates at time t of the Lagrangian fluid point location. Steps for solving the fluid displacement and velocities are explained in Figure 3.7a-d.

3.7 Lagrangian Mesh of the Vibrating Fan

The time-dependent Lagrangian mesh is constructed for each time step using the fiber model, allowing it to solve fully coupled fluid-structure interaction problems. Out of many fiber models used by Battista, Target points are implemented to model the flapping piezoelectric fan movement because this fiber model allows movement of rigid body at desired position. The coordinates for Lagrangian points are transformed through an interpolation function to a newly specified location. Each target point is connected to boundary points in the fluid-structure region via

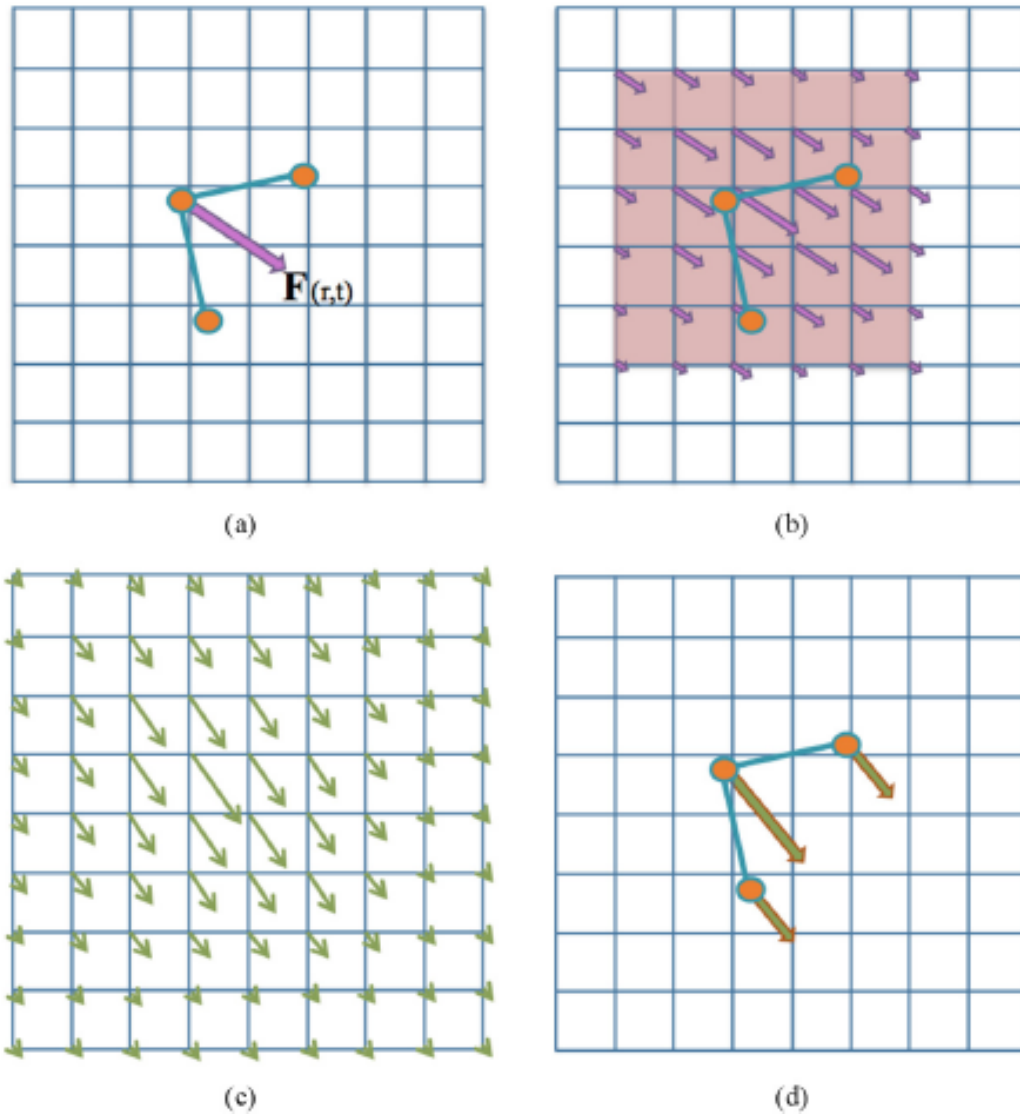


Figure 3.7: A brief guide to the basic steps in Peskin's immersed boundary method. **(a)** The elastic force of deformation is taken from the current configuration of the immersed structure. The force density $F^n(r, t)$ is calculated for n^{th} time step. **(b)** The force computed on immersed boundary is then distributed to the Lagrangian nodes of fluid points nearby with Equation 9. **(c)** Fluid velocity is updated everywhere on the computational domain with FFT method to solve Navier-Stokes Equation 8 **(d)** Fiber model position is updated to \mathbf{X}^{n+1} using local fluid velocities [7].

a stiff spring with zero resting length. Movements of Lagrangian target points immersed in the computational domain is shown in Figure 3.9.

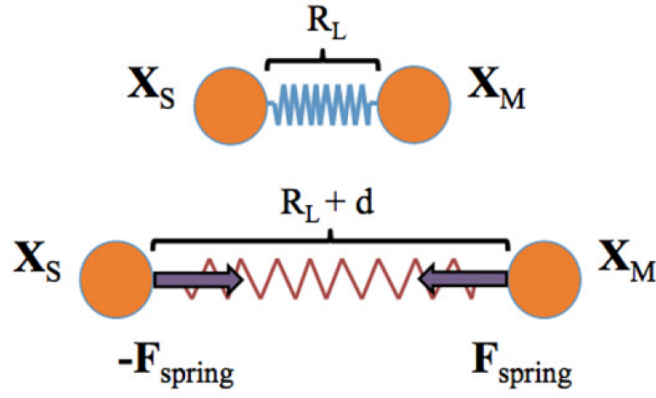


Figure 3.8: Two Lagrangian points connected by spring with zero resting length. F_{spring} is a result of the change in displacement on spring, d . Image courtesy of Battista [7].

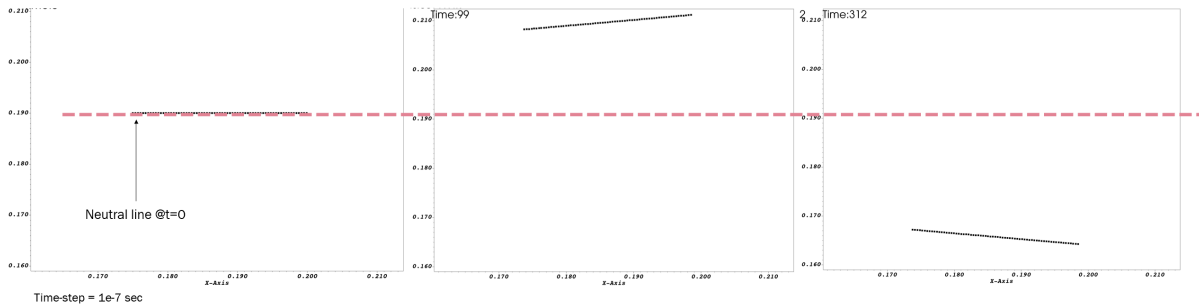


Figure 3.9: Zoomed in time-step illustration of immersed boundary of the fan. IB2d solves the discretized Navier-Stokes equation for each time step.

Leading edge: $2.535e - 3 * \sin(314.6 * t + 1.579)$

Trailing edge: $2.970e - 3 * \sin(302 * t + 1.664)$

3.8 Eulerian Mesh of the Fluid in Control Volume

IB2d utilizes delta function $\delta_h(x)$ to discretize Equation 9 and 10.

$$\delta_h(\mathbf{x}) = \frac{1}{h^2} \phi\left(\frac{x}{h}\right) \phi\left(\frac{y}{h}\right) \quad (11)$$

where Eulerian fluid grid width is denoted by h and

$$\phi(r) = \frac{1}{4} \left(1 + \cos\left(\frac{\pi r}{2}\right) \right) \quad (12)$$

for $|r|$, the absolute value of distance between Lagrangian and Eulerian node is less than or equal to 2 units of the lattice. The value for $\phi(r)$ is assumed 0 for $r > 2$. The fan is placed in center of $0.375m \times 0.375m$ computational domain to minimize any interface from the fixed walls. The length and width of computational domain is kept at least 10 times greater than the length of the immersed structure (0.025m). Courant Number is kept below 1 throughout the IB2d simulation. Zoomed in view of the full mesh is shown in Figure 3.11.

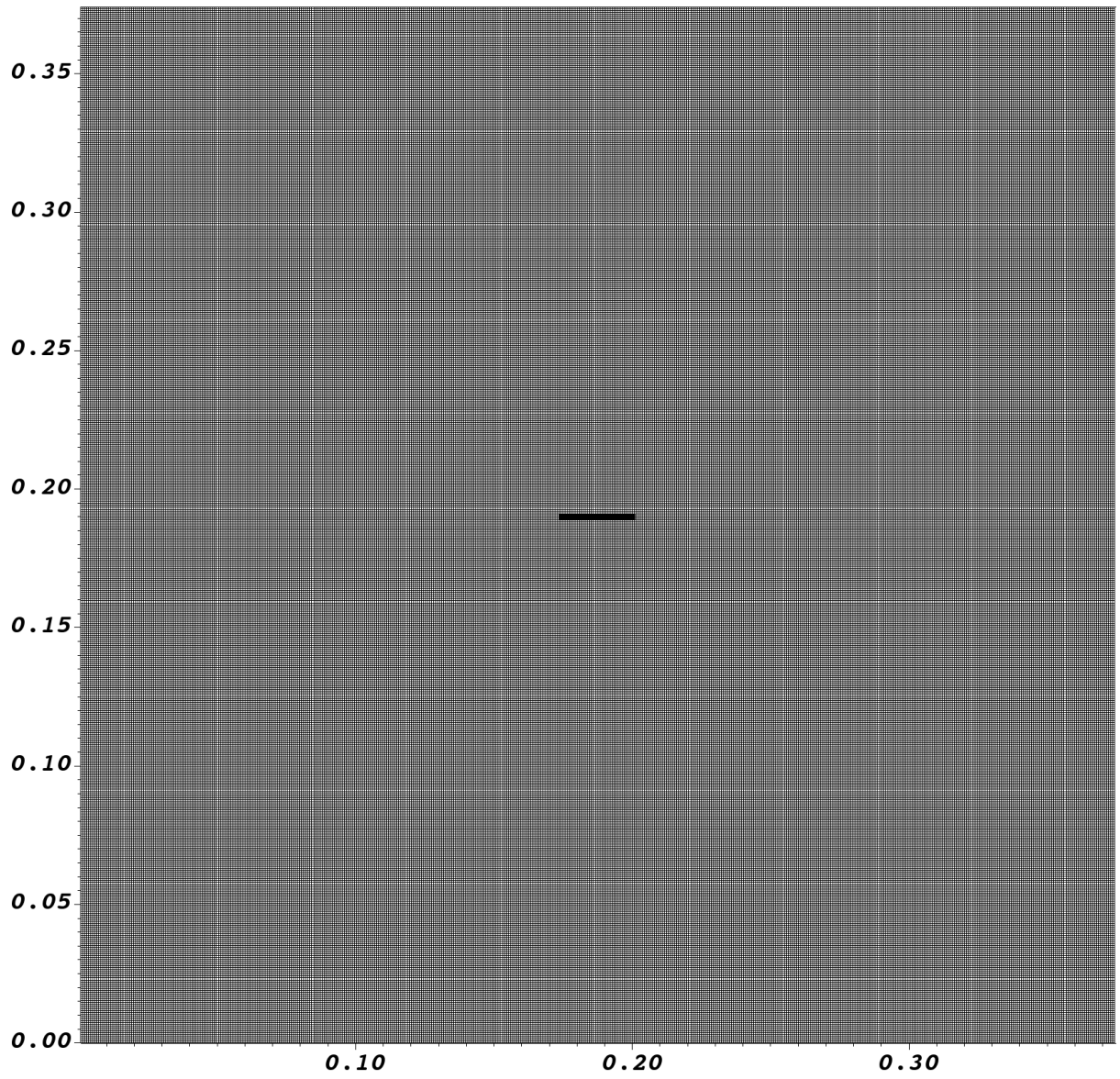


Figure 3.10: Mesh of the immersed boundary with 512×512 Eulerian grids.

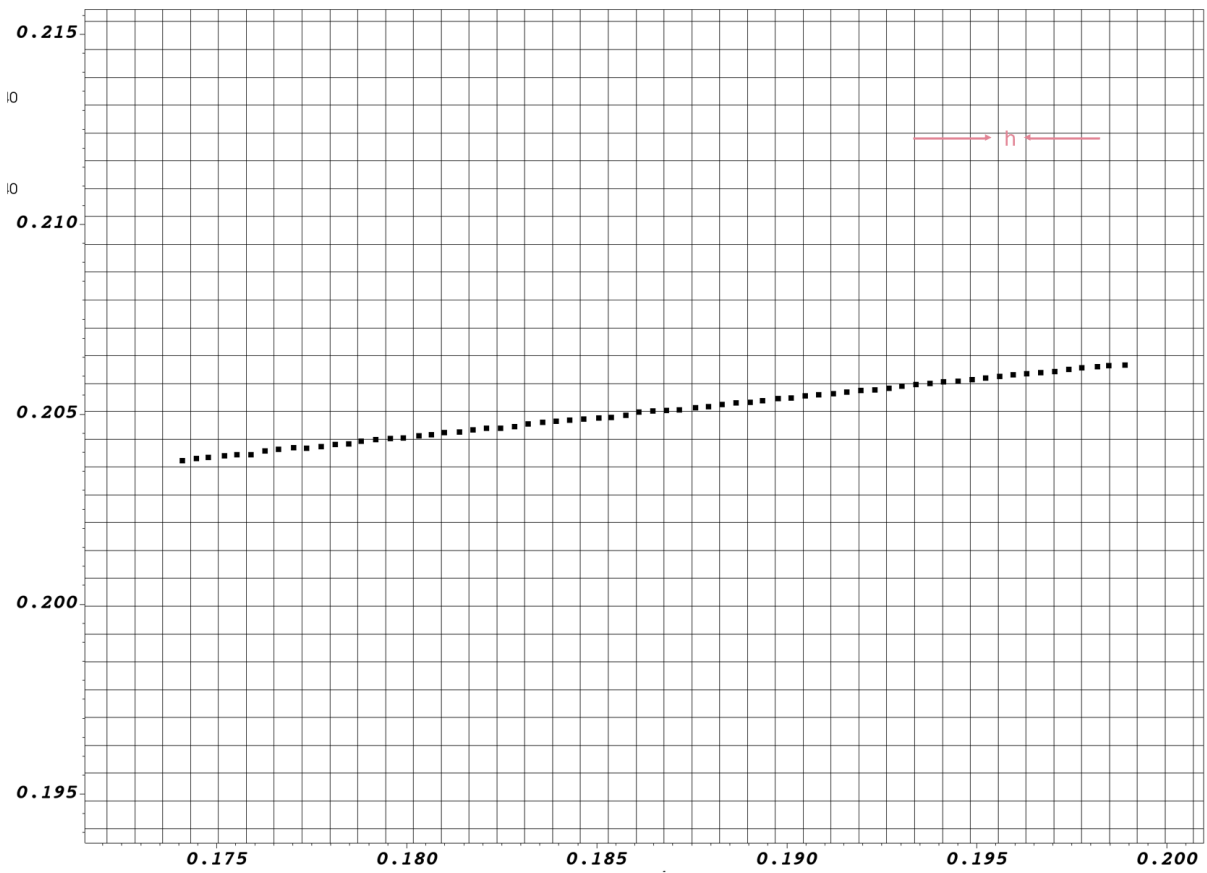


Figure 3.11: Zoomed in view of the IB mesh.

4 Results and Discussion

4.1 Vibration of the Fan

As expected, the oscillations of piezofan follows sinusoidal behavior. The best fit curve for blade's tip position is modeled: $A(t) = a \cdot \sin(bt + c)$. The coefficient for all voltages are shown in Table 3.

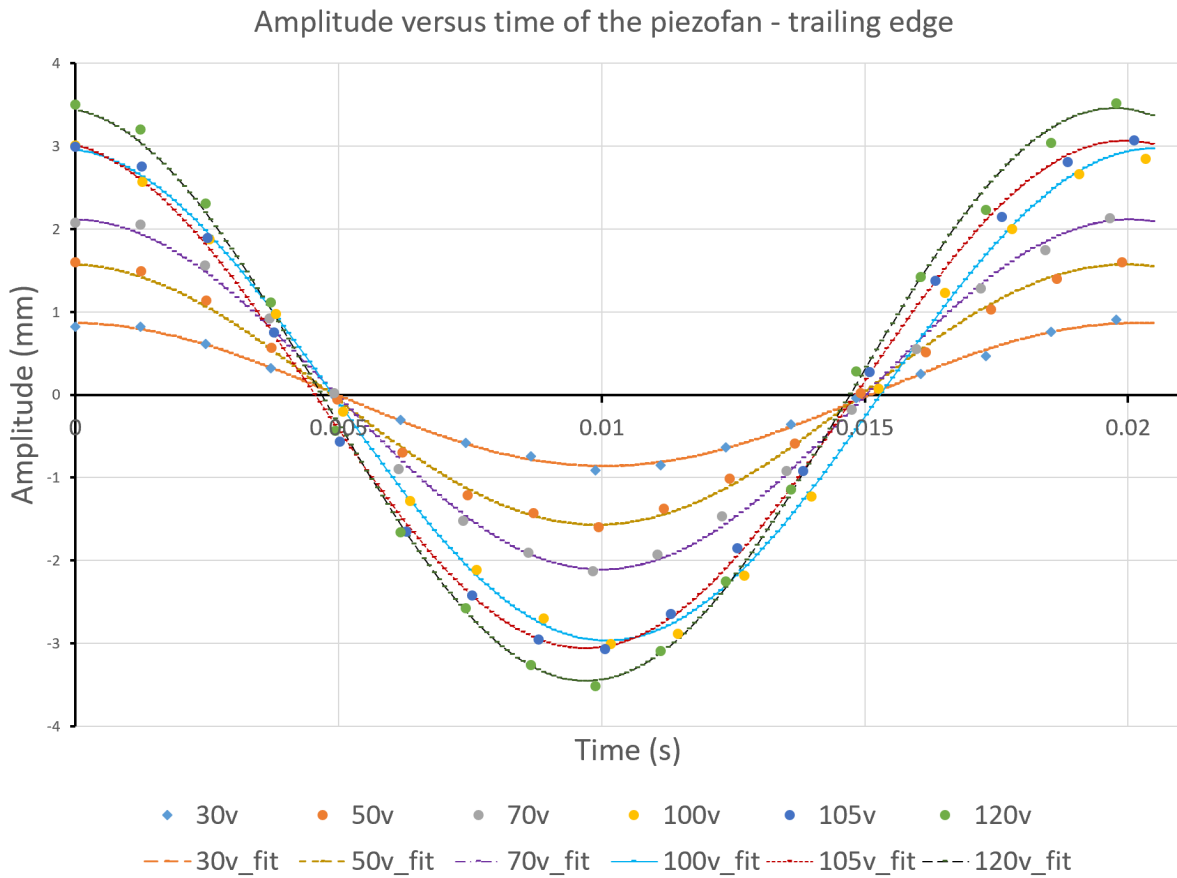


Figure 4.1: Fan-tip position of the trailing edge.

Table 3: Coefficient for the best fit sinusoidal curve of the trailing edge's tip.

Voltage (V)	$a(10^{-3}m)$	$b(1/s)$	$c(10^{-3}m)$	R^2
30.0	0.863	309.5	1.604	0.9969
50.0	1.57	312.0	1.624	0.9978
70.0	2.11	312.2	1.593	0.9976
100.0	2.97	302.0	1.664	0.9985
105.0	3.06	305.8	1.750	0.9987
120.0	3.46	312.9	1.678	0.9979

The average period of oscillation for all voltages is $19.92ms$ which translates to approximately $50Hz$ - the frequency of input to the piezo-actuator. Thus, the frequency of oscillation at which piezo-fan vibrates is found to have 1:1 relation with frequency of the AC power input.

4.2 Vortex Formation

Development of the boundary layer on the oscillating fan results in vortex shedding from leading edge to trailing edge of the fan. Vortex formation and detachment from the trailing edge of the fan occurs quicker as Reynold's Number increase.

For all Reynold's Number, counter-rotating vortices are generated at the tip during each cycle. On flow regime at lower Reynolds number ($Re < 250$), vortices generated travel as a

Table 4: Occurrence of fully developed vortex formation and detachment.

Re	t/T
72.40	3/4
131.8	5/8
177.2	5/8
249.1	1/2
281.8	1/8

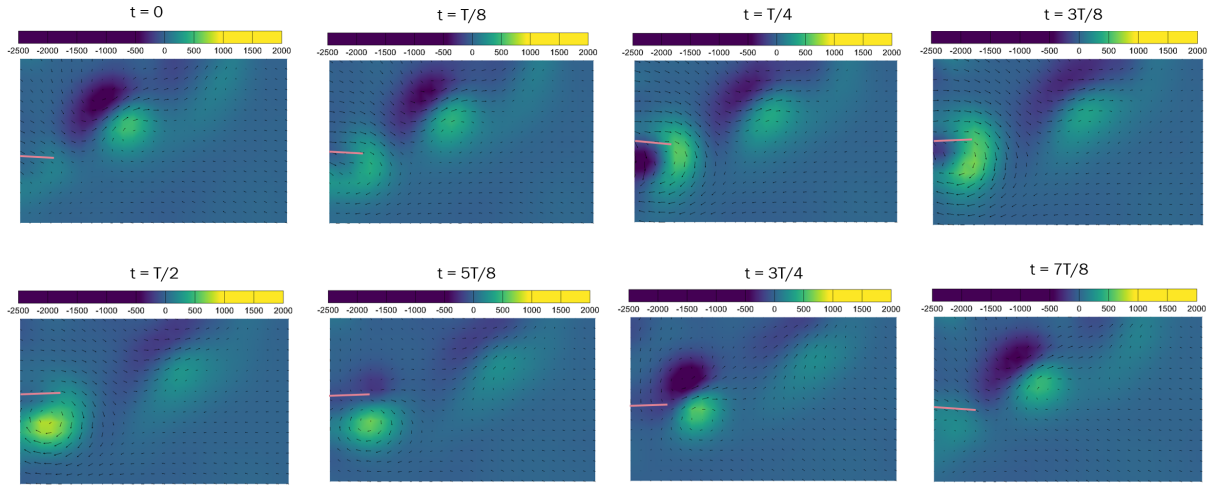


Figure 4.2: Time sequence of vortex ($1/s$) formation and evolution in the propagating regime at $Re = 72.4$

pair north-east and dissipate before they reach edges of the frame. The dissipation of vortices occur because the vibrating beam generates much lower circulation at lower Reynold's Number. This behavior is also observed by Emrahimi et al. [15]. Figure A.1 shows the time sequence of vortex formation and evolution at 30V 50Hz.

At higher Reynold's Number $Re > 250$, vortex pairs travel south-east at much higher magnitude and do not dissipate as they approach edges of the frame. The south-west trajectory path is also observed on numerical simulation and experimental results by Choi et al [19].

4.3 Circulation and Decay of Vortices

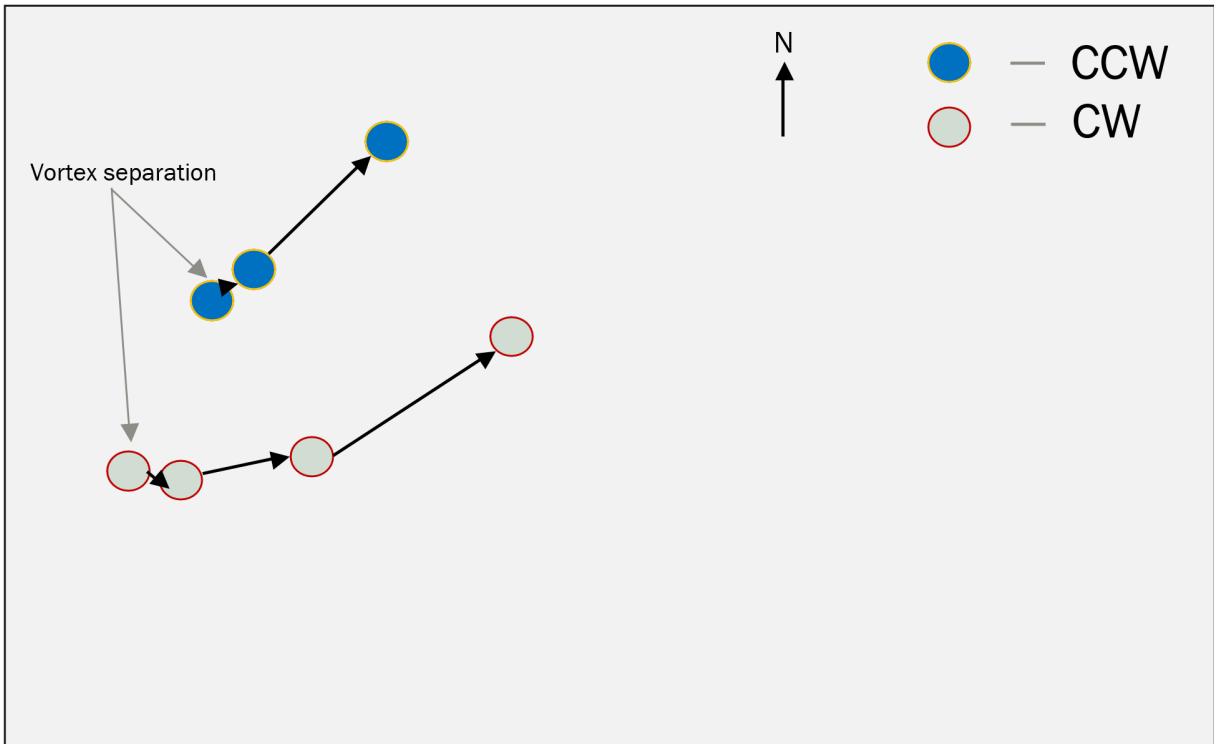


Figure 4.3: Vortex path from $t = 0T$ to $t = 7T/8$ for $Re = 72.4$

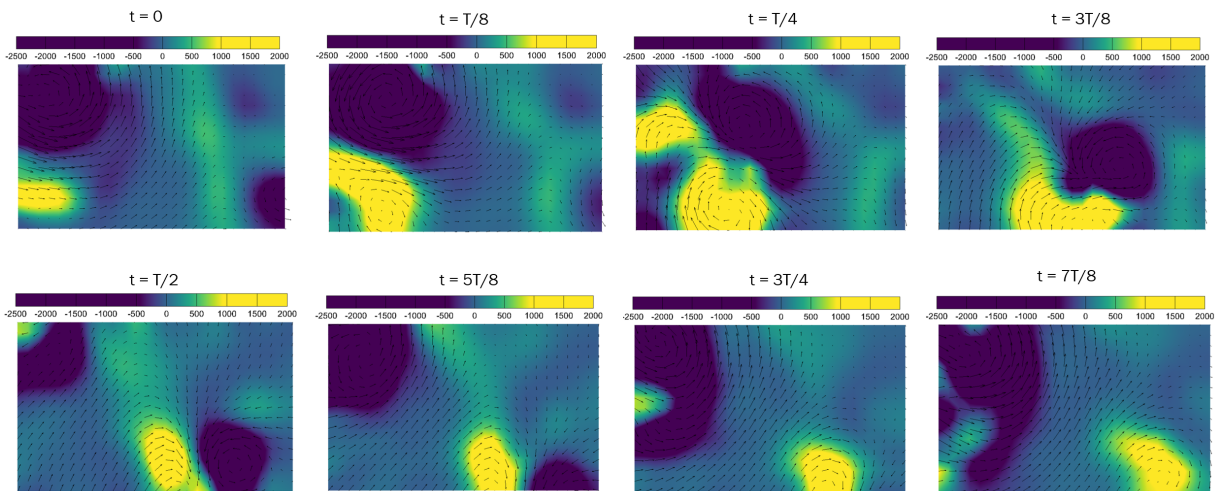


Figure 4.4: Time sequence of vortex ($1/s$) formation and evolution in the propagating regime at $Re = 281.8$

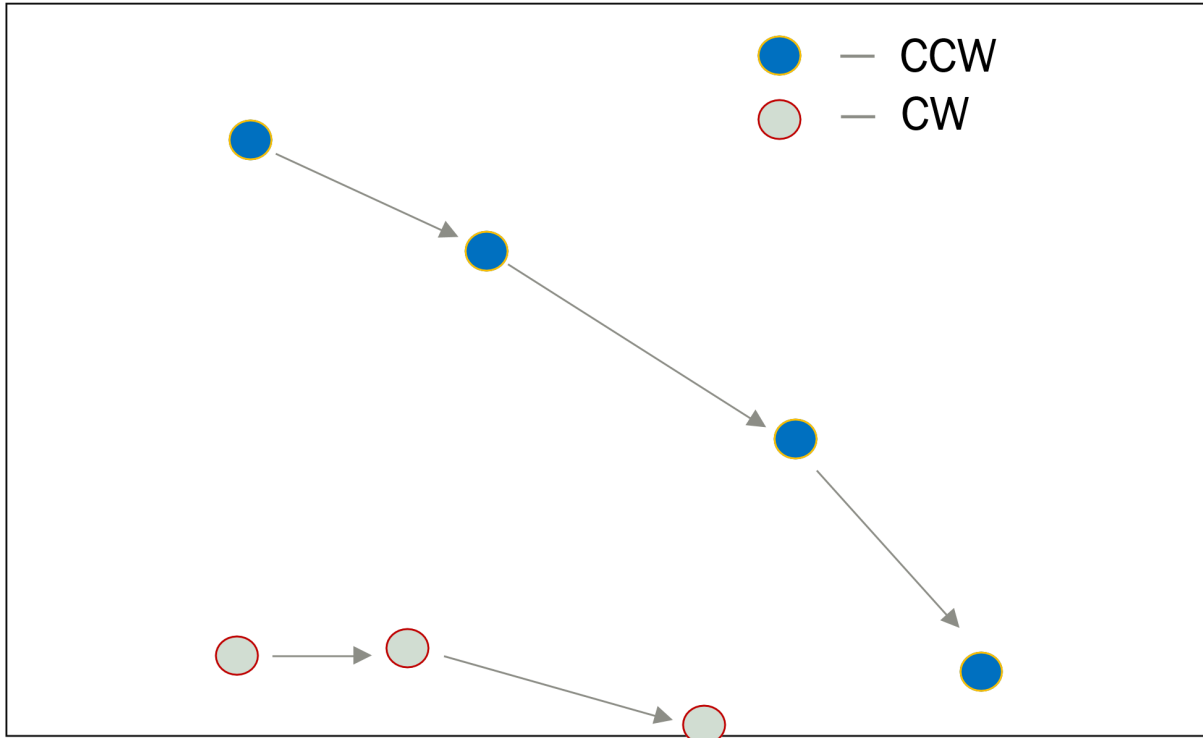
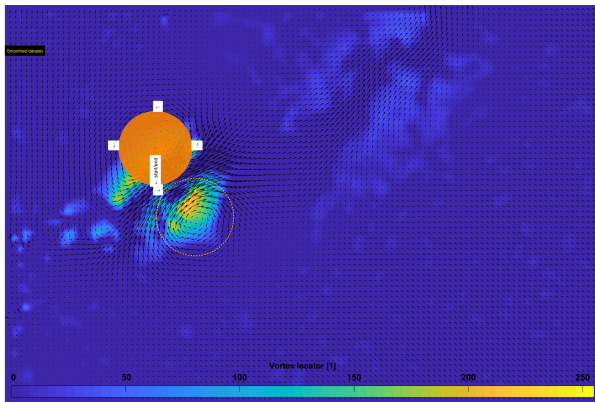
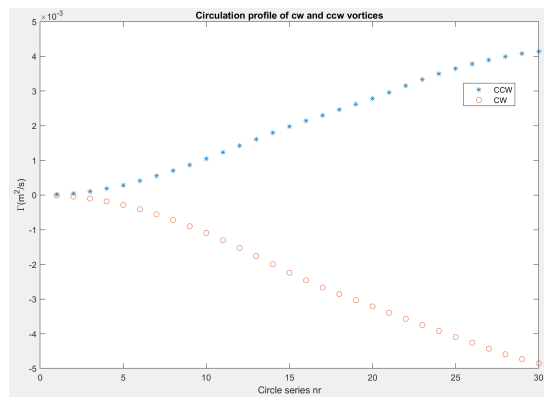


Figure 4.5: Vortex trajectory for 115V at 50Hz for one complete oscillation. $Re = 281.8$



(a) Series of 30 circles drawn around both pairs of vortex to calculate the circulation.



(b) Circulation profile around vortices.

Figure 4.6: Circulation of counter-rotating vortices at $t = T/8$. Power input = 30.0V

4.3.1 Vortex interactions

The interaction between two counter-rotating vortices greatly affect the velocity vectors. In contrary to the findings of [15], velocity magnitudes increase significantly in the overlapping regions between counter-rotating vortices. This increase in magnitude is contributed by the additions of velocity component in u direction.

The velocity in v -direction on the other hand in overlapping region cancel each other because Circulation ($\Gamma(t)$) for the vortex pair are negatives of one another.

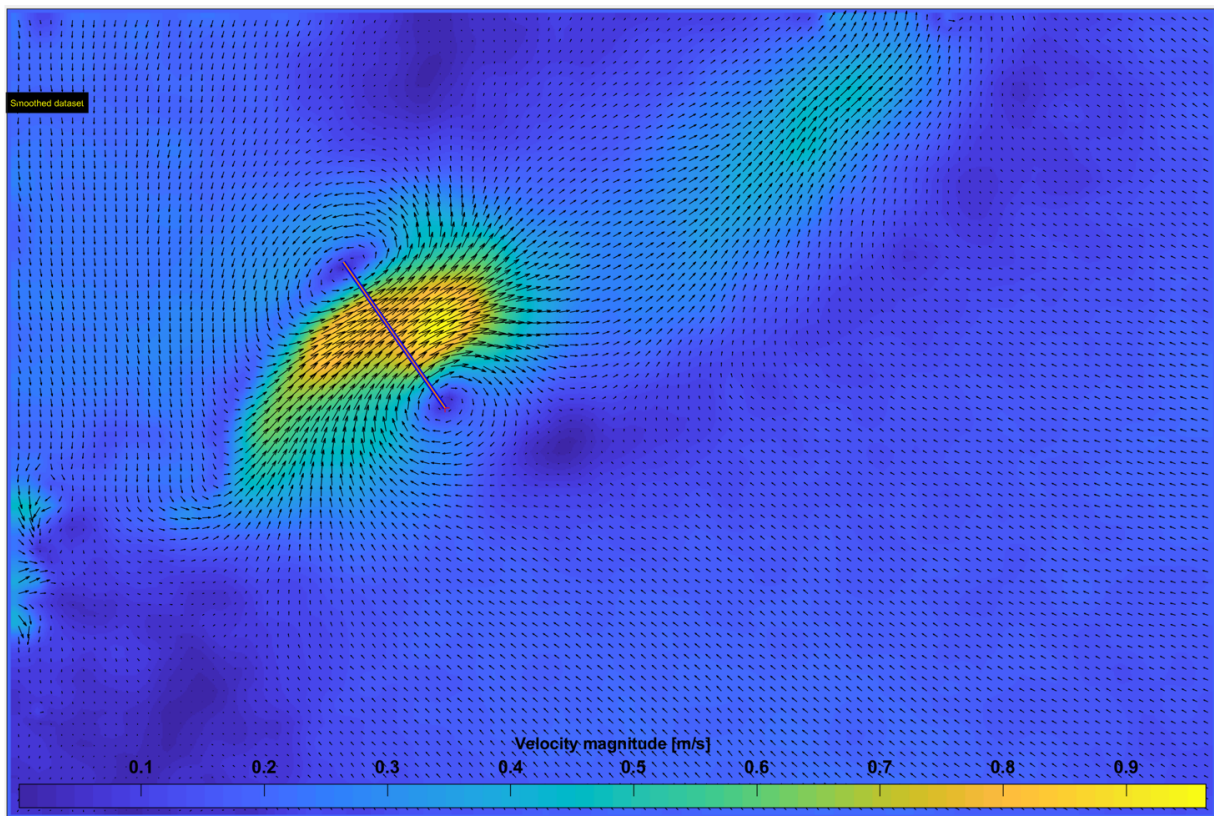


Figure 4.7: Velocity magnitude for power input of $30V$ at $50Hz$. Velocity profile across the overlapping region of counter-rotating vortices is plotted on Figure 4.8.

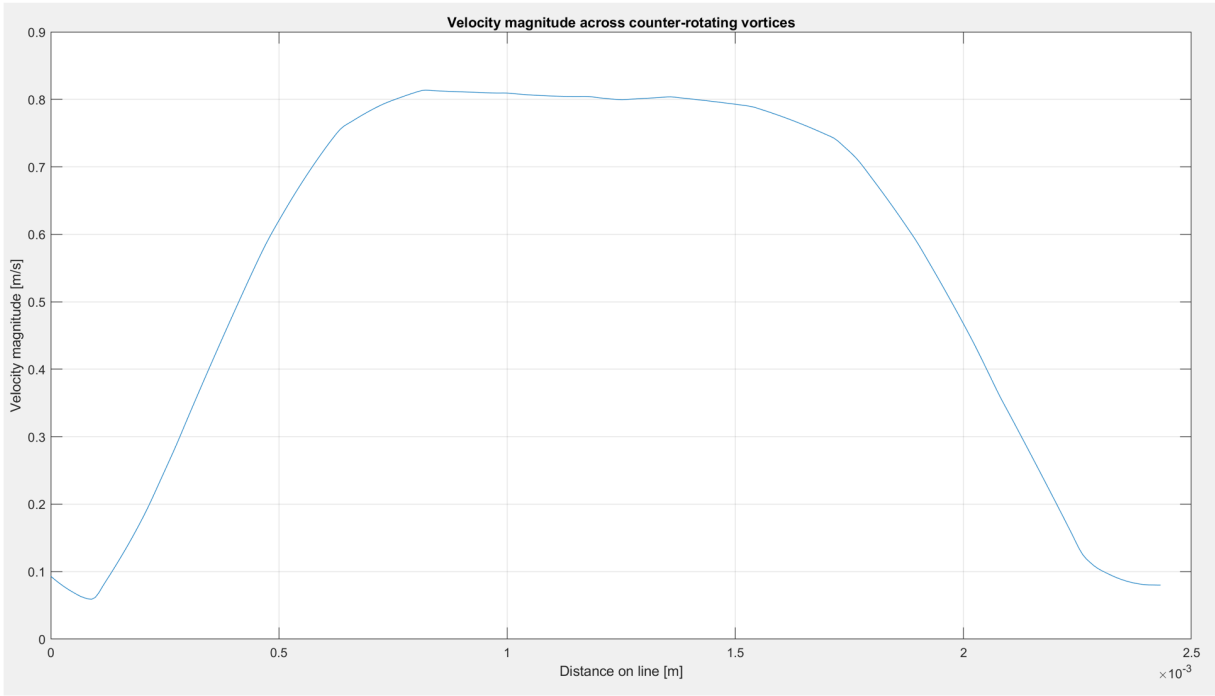
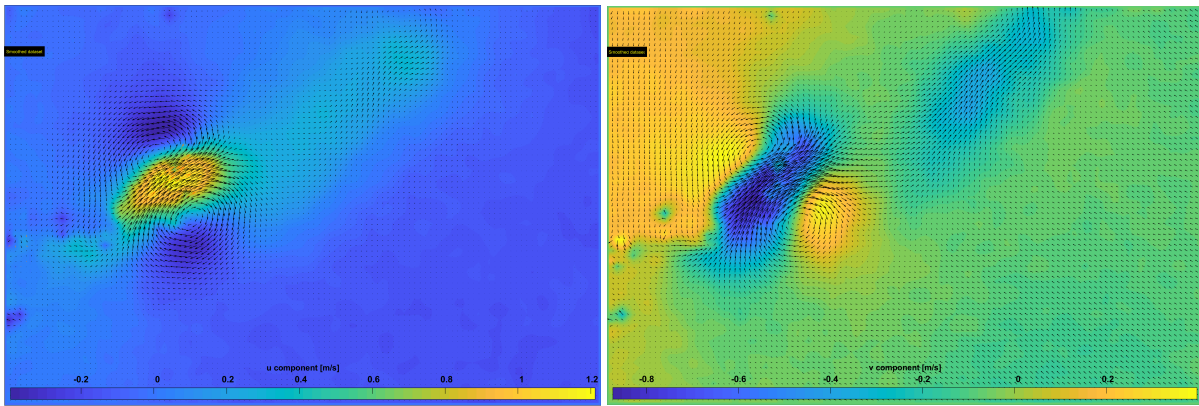


Figure 4.8: Velocity magnitude profile across the overlapping region.

4.3.2 Vortex decaying

The tangential velocities remain relatively constant at a given radius from the center of vortex. Gaussian velocity profile (shown in Figure 4.10) classifies the vortices in this experiment as Lamb-Oseen vortices, named after Horace Lamb and Carl Oseen. As vortex moves along the frame, its magnitude decreases due to the disturbances from fluid's viscosity [15].

The circulation reaches the maximum value significantly quicker over time for $Re > 100$ (at $t/T < 0.3$). $Re < 100$ on the other hand reaches its peak after $t = t/T$ surpasses 0.5. The oscillating behavior of $\Gamma(t/T)$ is most likely due interference between vortices generated at extreme points of the oscillation. The vortices shed from the leading edge of the fan also interfere with the vortices generated by the trailing edge. This phenomenon leads to periodic oscillation of tangential velocity in overlapping region. The fast decay in circulation over time is also observed by Kim et al. [20] and Ebrahimi [15]. This rapid decrease is most certainly due



(a) Velocity profile of u -component in overlapping vortex region. (b) Velocity profile of v -component in overlapping vortex region.

Figure 4.9: Instantaneous velocity components of two counter-rotating Lamb-Oseen vortices.

to the collision of flows in u -direction induced by counter-rotating vortices.

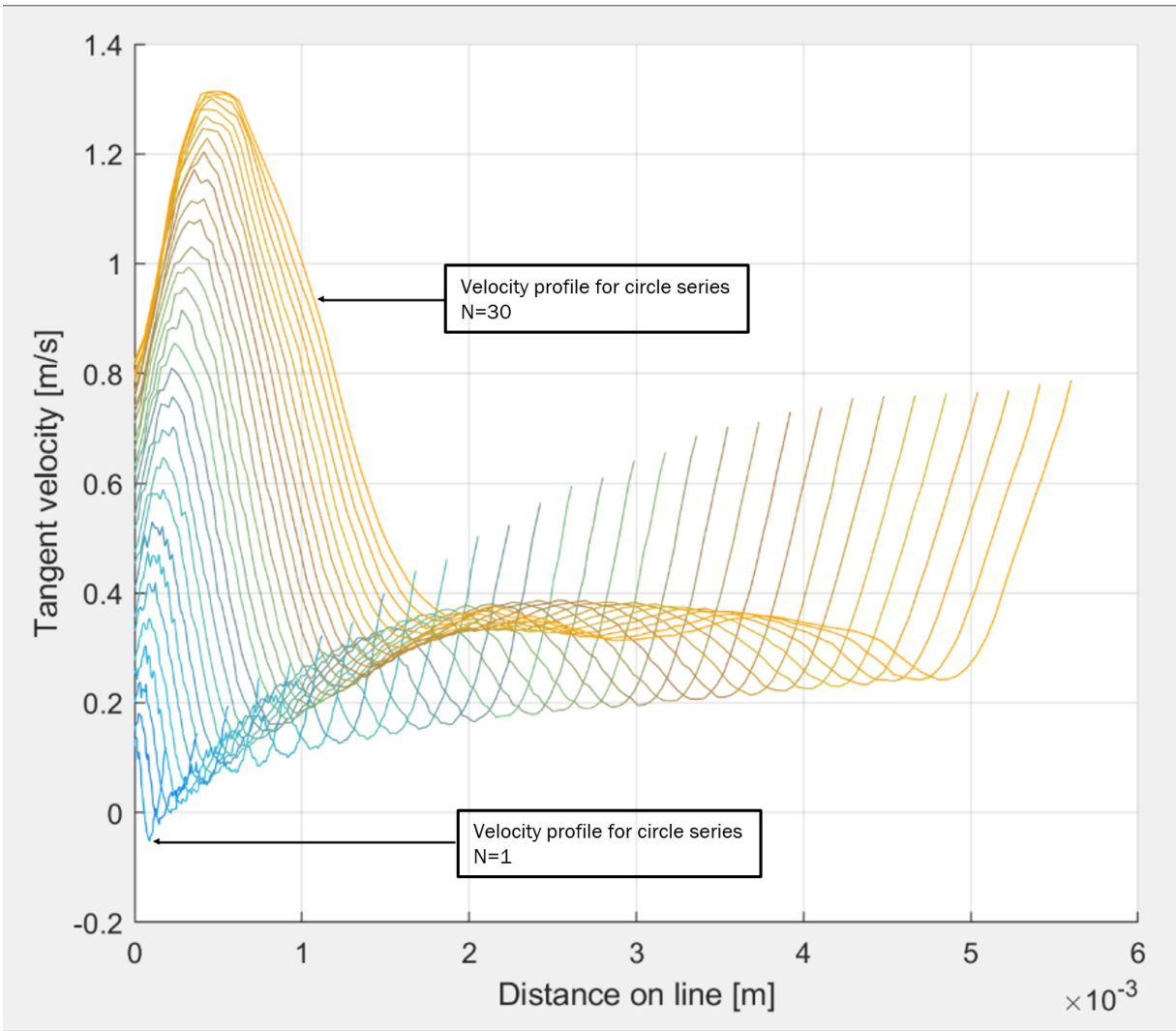


Figure 4.10: Tangential velocity profile of a CCW-rotating vortex. Refer to Figure 4.6a on how 30 concentric circles are drawn around a vortex.

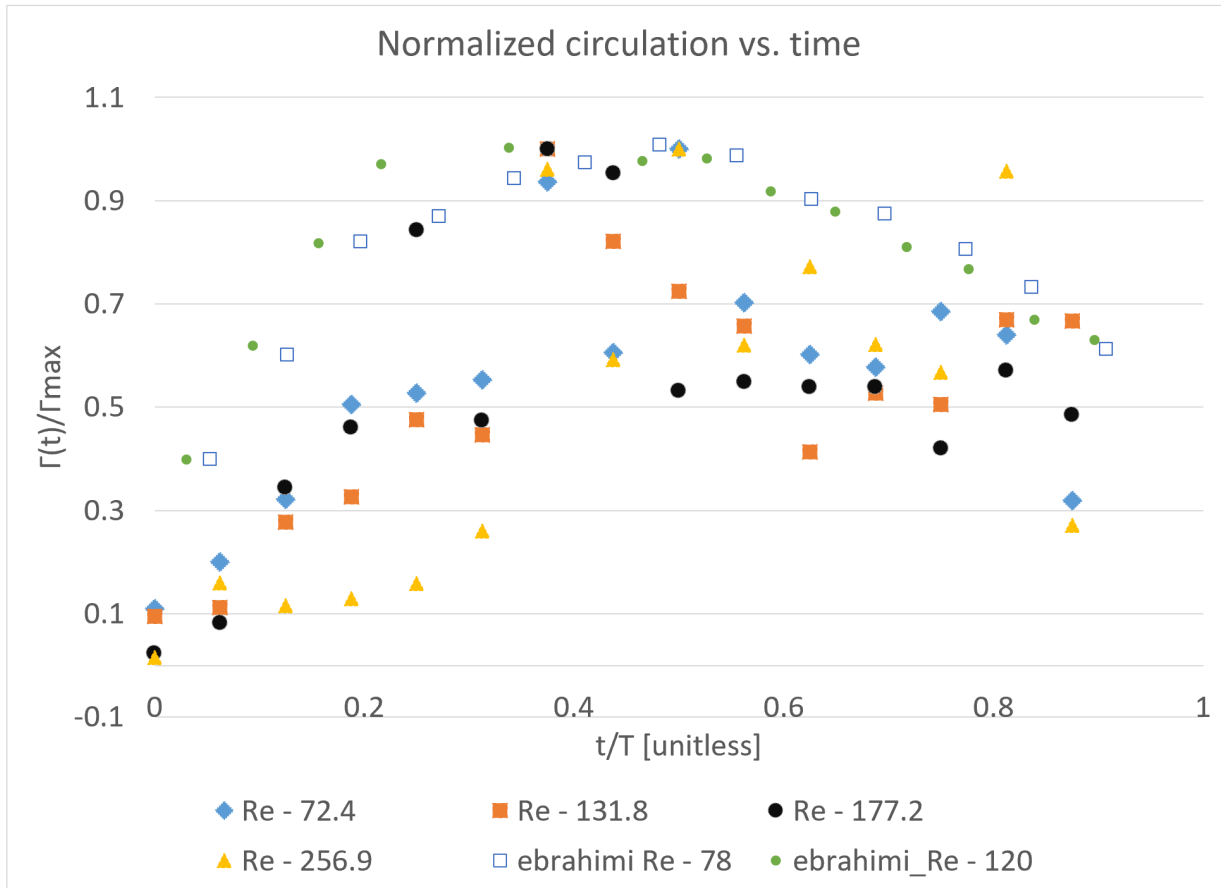


Figure 4.11: Normalized circulation around CW vortex in one cycle of oscillation as function of unitless t/T .

4.4 Uncertainty Analysis

Thieliecke 2014[25], the creator of PIVlab, estimated the uncertainty of $\sigma_{pix} = \pm 0.14$ pixel for each displacement vectors. The pixel to real-length using from calibration image, $P_r = 5.4432 \times 10^4$ pixel/m. With these values, the uncertainty in displacement pertinent to this experiment can be calculated with Equation 13.

$$\begin{aligned}\sigma_x &= \frac{\sigma_{pix}}{P_r} \\ &= \frac{0.14pix}{5.4432 \times 10^4 pixel/m} \\ &= 2.57 \times 10^{-6}m\end{aligned}\tag{13}$$

Since time-step $\Delta t = 1.1364 \times 10^{-3}$ seconds, the uncertainty in velocity σ_V can be estimated:

$$\begin{aligned}\sigma_V &= \frac{\sigma_x}{\Delta t} \\ &= \pm 0.0226m/s\end{aligned}$$

Hence, the uncertainty of velocity vectors is estimated ± 0.0226 m/s.

4.5 Immersed Boundary Methods

As expected, pressure on top and bottom of the fan when they are on extreme points of oscillation are negatives of one another. In the beginning of simulation at time-step = 2, the pressure is at maximum. The magnitude of pressure also decreases as the fan reaches the upper extreme points as shown in Figure 4.12-4.14.

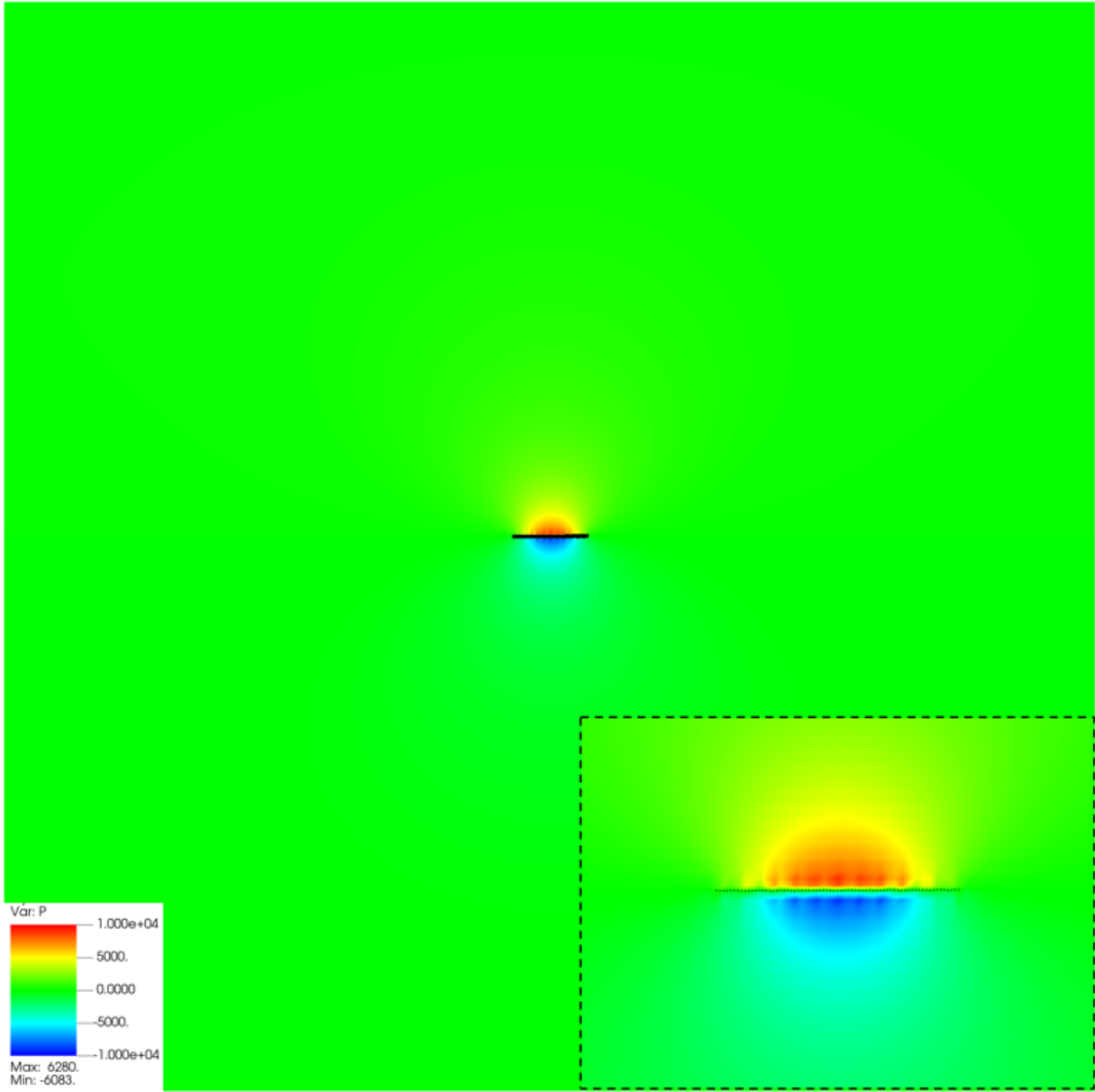


Figure 4.12: Pressure across the immersed boundary at time step = 2 ($t = 2 \times 10^{-7}$ seconds.)

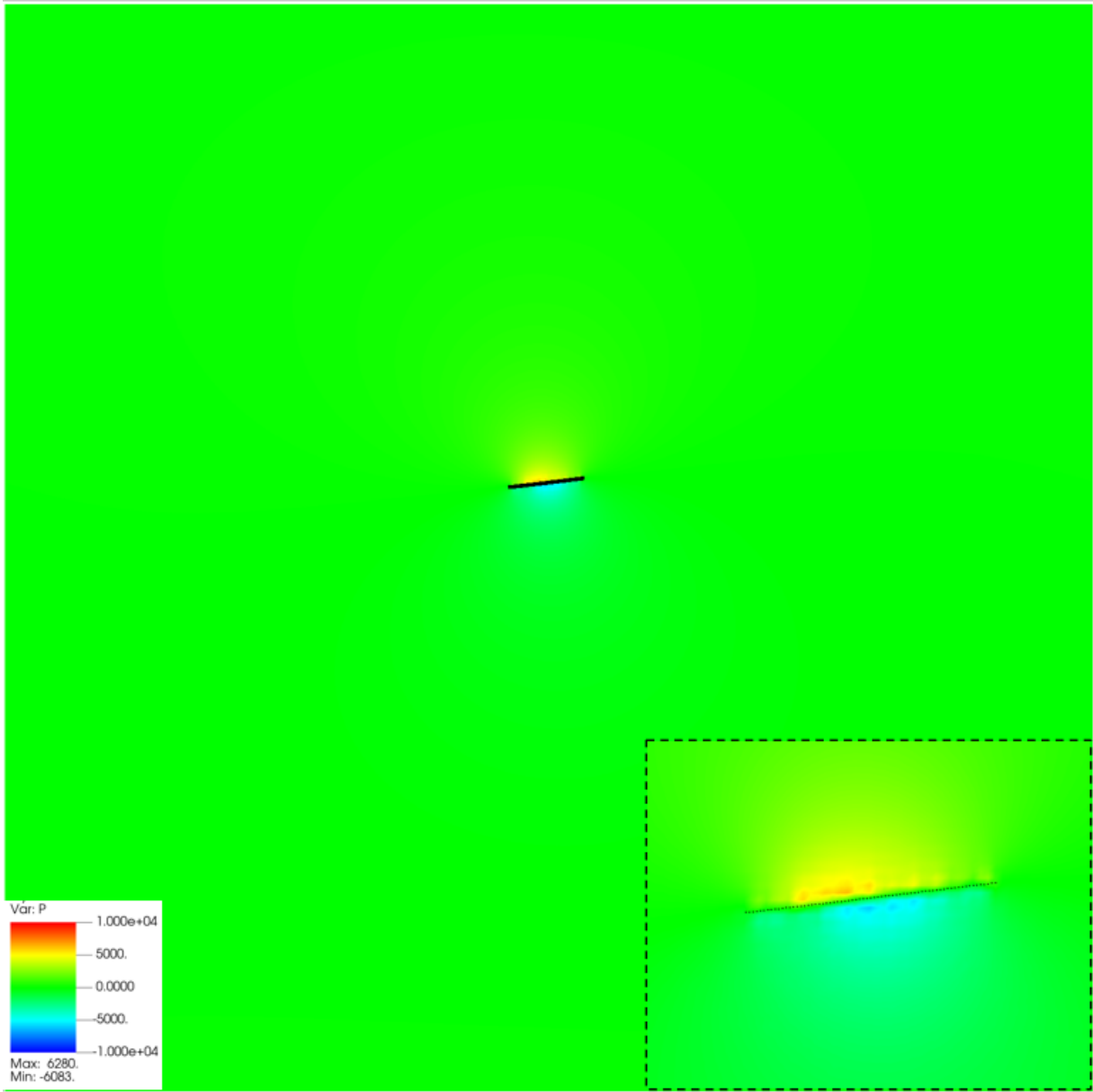


Figure 4.13: Pressure across the immersed boundary at $t = 99 \times 10^{-7}$ seconds.

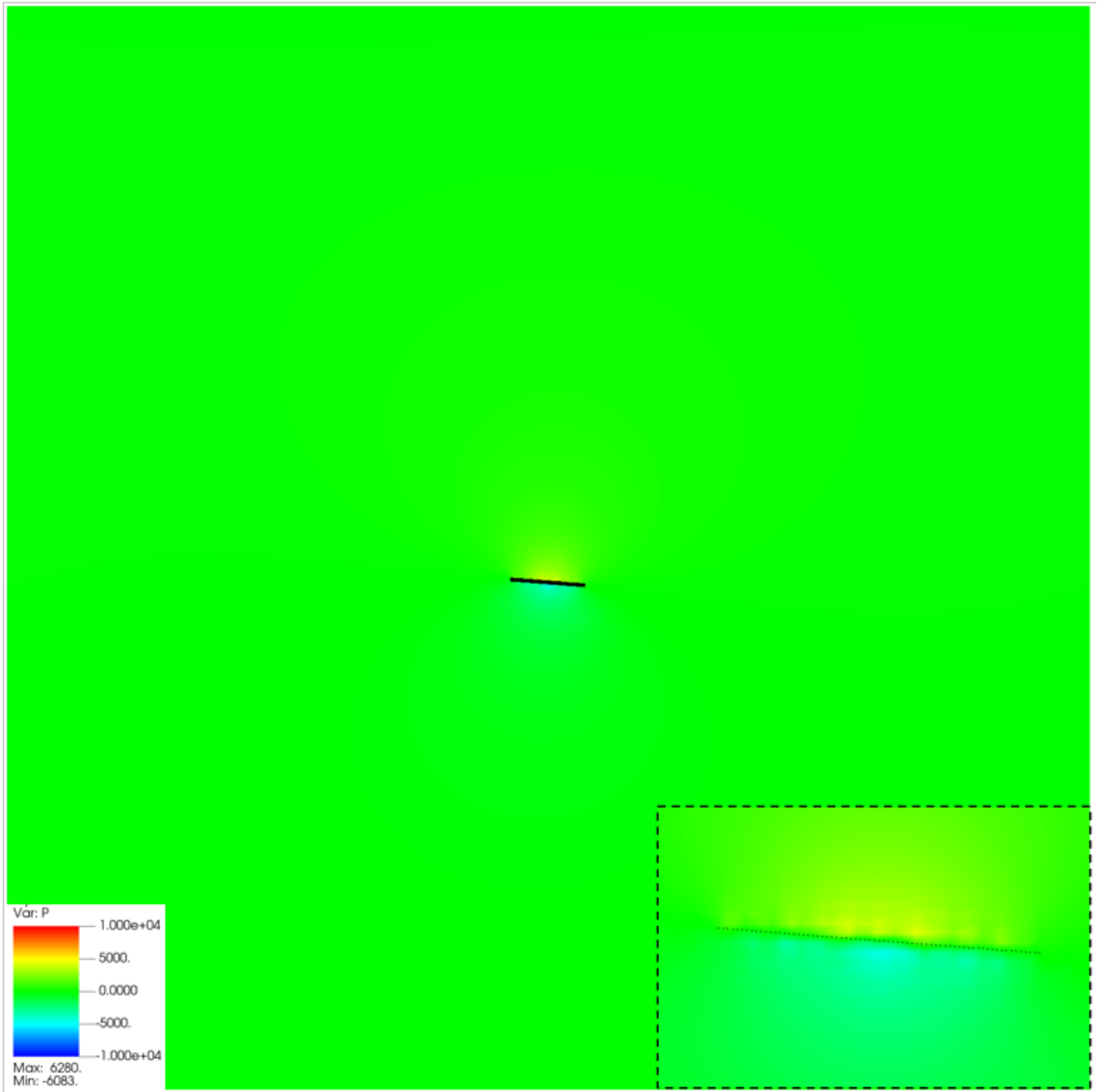


Figure 4.14: Pressure across the immersed boundary at $t = 369 \times 10^{-7}$ seconds.

The traces of vortex generated on the immersed structure with IB2d are not as fully defined as the experimental data. PIV analysis yielded maximum vorticity of $2000/s$ for power input of 100V at 50Hz whereas the immersed boundary method produced the maximum vorticity of $40000/s$ - an enormous difference between the two results.

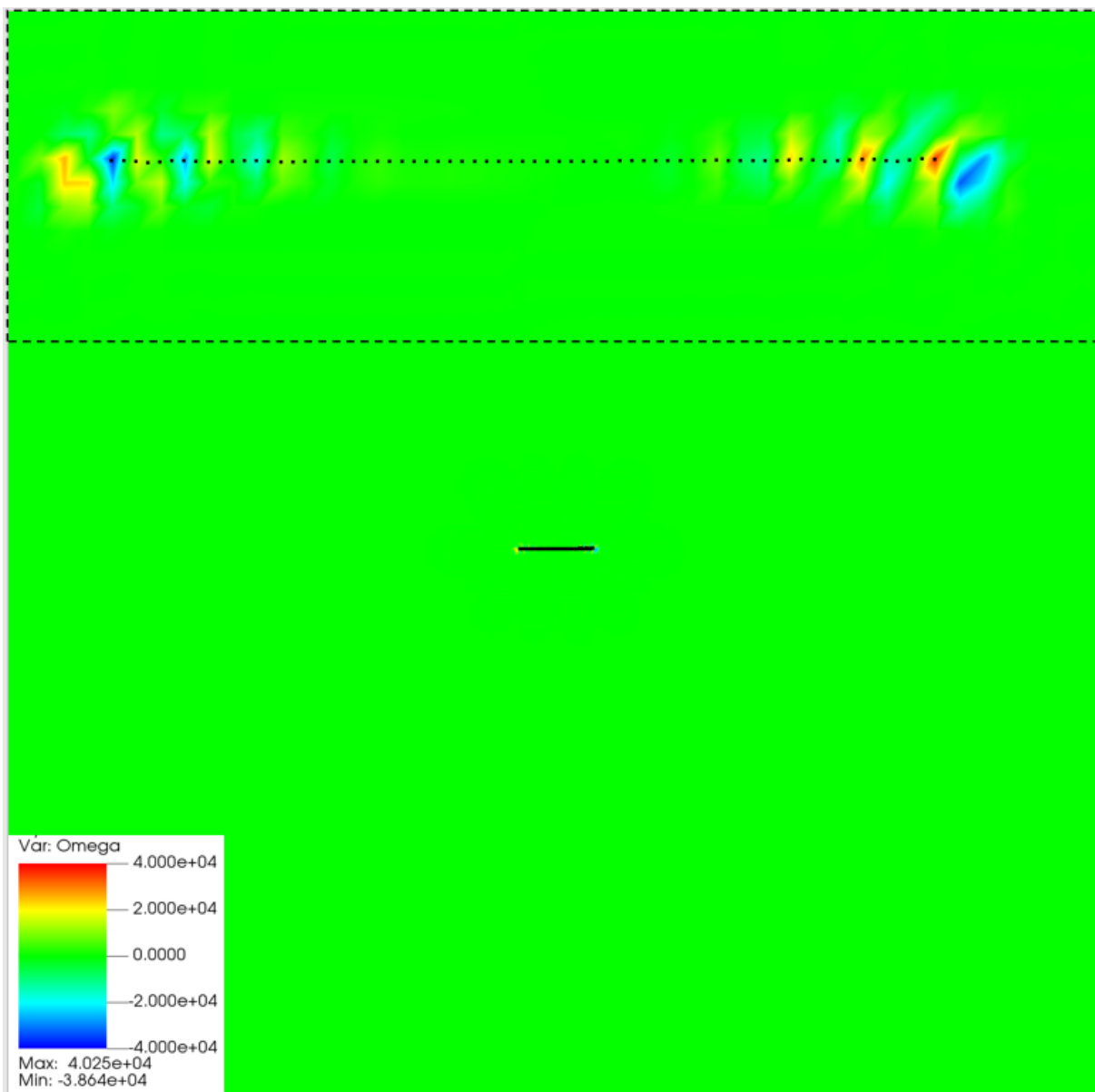


Figure 4.15: Vortices across the immersed boundary at time step = 2 ($t = 2 \times 10^{-7}$ seconds.)

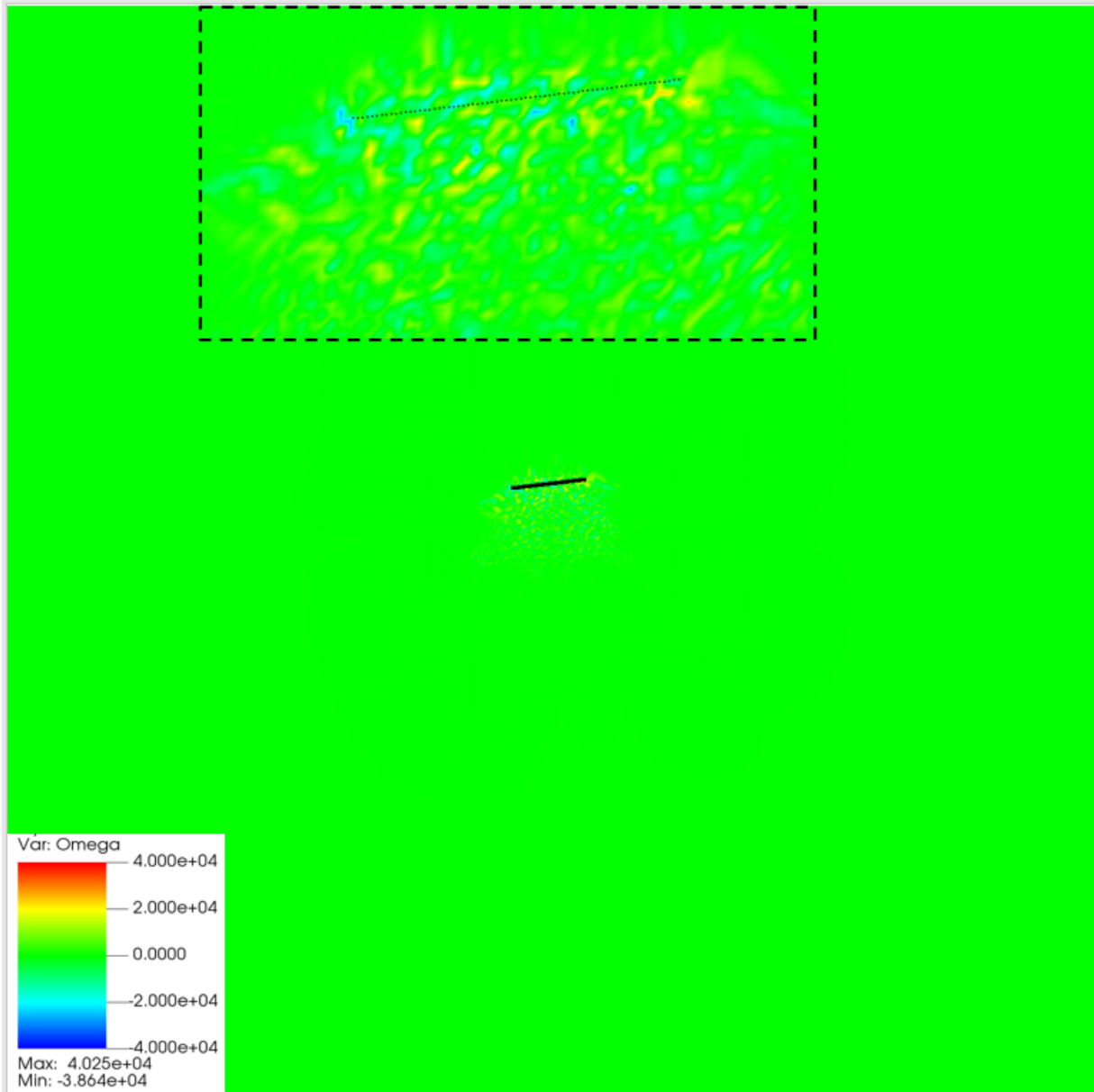


Figure 4.16: Vortices across the immersed boundary at $t = 99 \times 10^{-7}$ seconds.

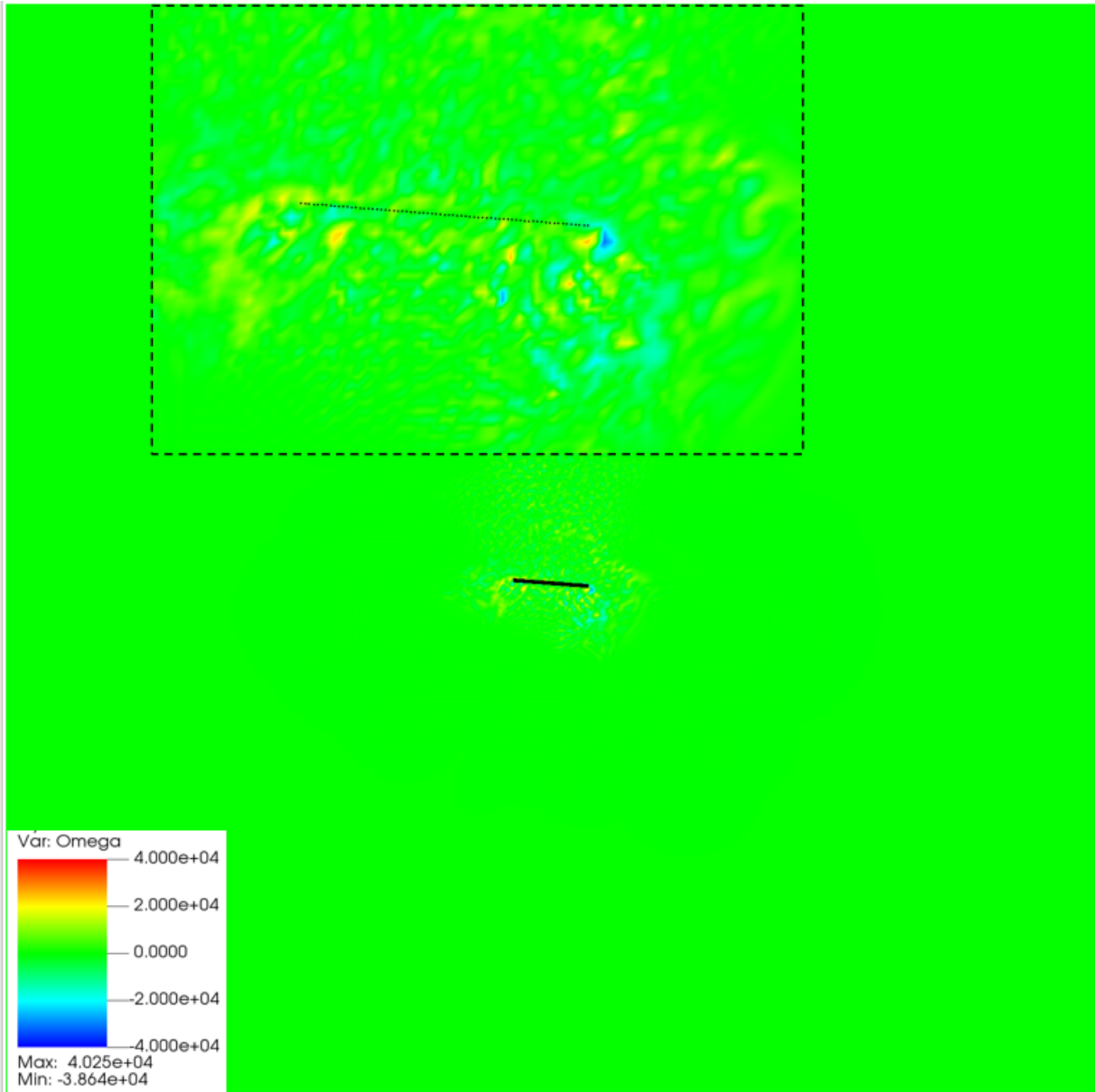


Figure 4.17: Vortices across the immersed boundary at $t = 369 \times 10^{-7}$ seconds.

5 Conclusions and Recommendations

In this thesis, fluid behavior across a vibrating piezoelectric fan on a in-compressible and viscous fluid domain is examined with power input ranges between 30.0V and 120.0V. For each cycle of oscillation, a pair of counter-rotating vortices are generated due to the formation of boundary layer. The trajectory and distance between the counter rotating vortices are affected by Reynolds Number. For $Re < 250$, vortex pair propagate and travel upward where as for $Re > 250$, the vortex pair propagate downward. Vortex generated within a same cycle travel farther apart from one-another with an increase in Reynold's number. Over time, circulations around vortices generated at low power input (low Re) decrease more drastically than vortices at higher power input (high Re).

Asymmetry is observed in the trajectories of all counter-rotating vortex pairs for all Reynold's numbers. Asymmetric vortex path is most likely desired by the manufacturer of the Bimitech fan when it was designed. However, asymmetric vortex paths have been observed as a result of inadequate clamping of the PZT actuator by [15] for low Reynold's number flows. Findings on vortex behavior from this thesis can be used to optimize the maximum fluid flow across piezofan. The uncertainty in velocity magnitude is calculated to be ± 0.0226 m/s for PIV measurements. The accuracy of PIV results decreases with an increase in the mean diameter of seeded particle [27]. Accuracy of results for flow attributes can be further improved by employing a higher resolution imaging system. The amount of noise from image sensor can hardly be quantified. There were several instances in PIV analyses where DFT failed to correlate the movement of seeding particles. This resulted in small regions of images missing displacement vectors. The noise on images are primarily caused due to uneven lighting throughout the frame. For future

experiments, inadequate lighting can be resolved by implementing multiple light sources from at-least two directions. Reflection of laser from the acrylic plate was observed on sequence of images. This issue can be mitigated by attaching a polarized filter on the lens.

Major discrepancy is observed between the experimental and simulation results when comparing vortices generated across the piezoelectric fan. The discrepancy is likely due to convergence issue even at the time step of 1×10^{-7} seconds. The error in IB2d simulation is likely due to non-convergence because the time-step (even at 1×10^{-7} seconds) is enormous for 512×512 Eulerian grid. With regards to computational costs, grid size should not be implemented beyond 512×512 [7]. Likewise, the time-step also should not be decreased below 1×10^{-6} seconds. More work is needed to correctly setup the FSI boundary condition so realistic results can be achieved. For users that are beginners in CFD, a GUI friendly software package such as ANSYS or COMSOL, as opposed to script based solver, could be more efficient and viable alternatives to solve FSI problems.

Bibliography

- [1] G. Gilson, S. Pickering, D. Hann, and C. Gerada, “Piezoelectric fan cooling: A novel high reliability electric machine thermal management solution,” *Industrial Electronics, IEEE Transactions on*, vol. 60, pp. 4841–4851, 11 2013.
- [2] J. G. KOOMEY, “Worldwide electricity used in data centers,” *Environmental Research Letters*, vol. 3, p. 034008, July 2008.
- [3] J. G. KOOMEY, “Growth in data center electricity use 2005 to 2010,” *Analytics Press*, Aug 2011.
- [4] “New technologies architectures for efficient data centers,” 2015.
- [5] Y. F. SITTI, M. CAMPOLO, D. *Development of PZT and PZN-PT based unimorph actuators for micromechanical flapping mechanisms*, vol. 4. 2001.
- [6] A. Borgoltz, “Particle image velocimetry.”
- [7] N. A. Battista, W. C. Strickland, and L. A. Miller, “IB2d : a python and MATLAB implementation of the immersed boundary method,” *Bioinspiration & Biomimetics*, vol. 12, p. 036003, mar 2017.
- [8] L. MA, H., SU, H.C., “Investigation of a piezoelectric fan cooling system with multiple magnetic fans,” *Sensors and Actuators A: Physical*, vol. 189, p. 356–363, 01 2013.
- [9] M. L. Kimber, “Thermal and fluidic characterization of piezoelectrically driven cantilevers,” *Purdue University*, Aug 2008.
- [10] S. ZHANG, “Numerical simulations and optimization analysis of the heat transfer in piezoelectric fans,” *Queen Mary University of London*, Sep 2018.
- [11] C. MANBACHI, Amir , “Development and application of piezoelectric materials for ultrasound generation and detection,” *Ultrasound*, vol. 19, no. 4, pp. 187–196, 2011.
- [12] “Perseus digital library,” 2020.
- [13] M. A. BIDAkhVIDI, “The design of a piezoelectric fan system for the flapping wing micro-air-vehicle application,” *Vrije Universiteit Brussel*, 2009.
- [14] M. Maaspuro, “Piezoelectric oscillating cantilever fan for thermal management of electronics and leds — a review,” *Microelectronics Reliability*, vol. 63, p. 342–353, 2016.
- [15] E. EBRAHIMI, Navid Dehdari and JU, Y. Sungtaek, “Wake vortex regimes of a pitching cantilever plate in quiescent air and their correlation with mean flow generation,” *Journal of Fluids and Structures*, vol. 84, p. 408–420, Jan 2019.
- [16] M. OKORIE, David, “Electricity consumption and economic growth: The nigerian case,” 12 2016.
- [17] J. Birch, W. Dickson, and M. Dickinson, “Force production and flow structure of the leading edge vortex on flapping wings at high and low reynolds numbers,” *The Journal of experimental biology*, vol. 207, pp. 1063–72, 04 2004.

- [18] N. Jeffers, K. Nolan, J. Stafford, and B. Donnelly, “High fidelity phase locked PIV measurements analysing the flow fields surrounding an oscillating piezoelectric fan,” *Journal of Physics: Conference Series*, vol. 525, p. 012013, jul 2014.
- [19] M. Choi, C. Cierpka, and Y.-H. Kim, “Vortex formation by a vibrating cantilever,” *Journal of Fluids and Structures*, vol. 31, p. 67–78, 2012.
- [20] Y.-H. Kim, S. T. Wereley, and C.-H. Chun, “Phase-resolved flow field produced by a vibrating cantilever plate between two endplates,” *Physics of Fluids*, vol. 16, no. 1, p. 145–162, 2004.
- [21] Y.-H. KIM, C. CIERPKA, and S. T. WERELEY, “Flow field around a vibrating cantilever: coherent structure eduction by continuous wavelet transform and proper orthogonal decomposition,” *Journal of Fluid Mechanics*, vol. 669, p. 584–606, 2011.
- [22] S. V. BIDAkhVIDI, Mohammad, SHIRZADEH, Rasoul, “Experimental study of the flow field induced by a resonating piezoelectric flapping wing,” *Experiments in Fluids*, vol. 54, 10 2013.
- [23] G. Elsinga, F. Scarano, B. Wieneke, and B. Oudheusden, “Tomographic particle image velocimetry,” *Experiments in Fluids*, vol. 41, pp. 933–947, 12 2006.
- [24] “Measurement principles of piv - dantec dynamics: Precision measurement systems sensors.”
- [25] S. Thielicke, W., “Pivlab – towards user-friendly, affordable and accurate digital particle image velocimetry in matlab. journal of open research software,” vol. 2(1), p. e30, 2014.
- [26] H. Chen, J.-S. Wang, C. Chen, S.-X. Liu, and H.-P. Chen, “Dynamic modeling and characteristic analysis of cantilever piezoelectric bimorph,” *Mathematical Problems in Engineering*, vol. 2019, p. 1–9, Mar 2019.
- [27] W. Thielicke, “The flapping flight of birds analysis and application phd thesis,” *University of Groningen*, 2014.
- [28] W. THIELICKE, “Pivlab - digital particle image velocimetry tool for matlab.” url: <https://pivlab.blogspot.com/>, 2014. Accessed: 08-05-2020.

Appendix A Vorticity Plots for all Voltages

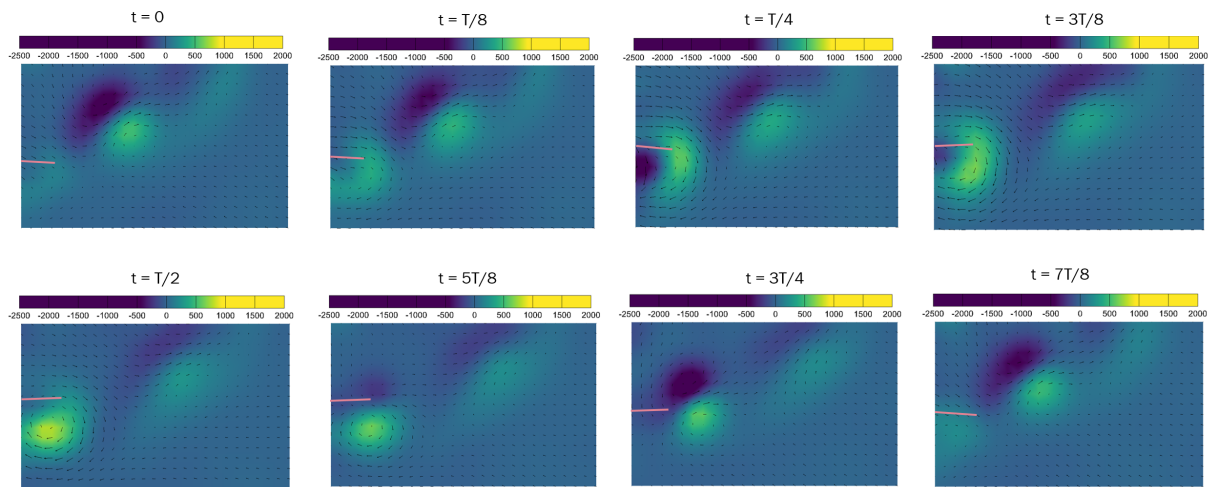


Figure A.1: Time sequence of vortex ($1/s$) formation and evolution in the propagating regime at $Re = 72.4$. Power input = 30V 50Hz.

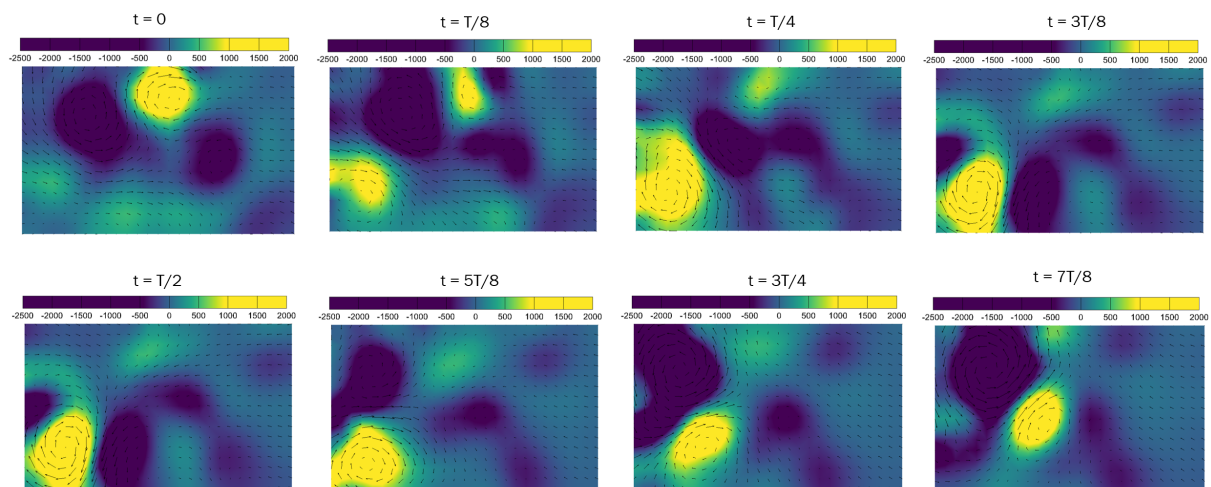


Figure A.2: Time sequence of vortex ($1/s$) formation and evolution in the propagating regime at $Re = 131.8$. Power input = 50V 50Hz.

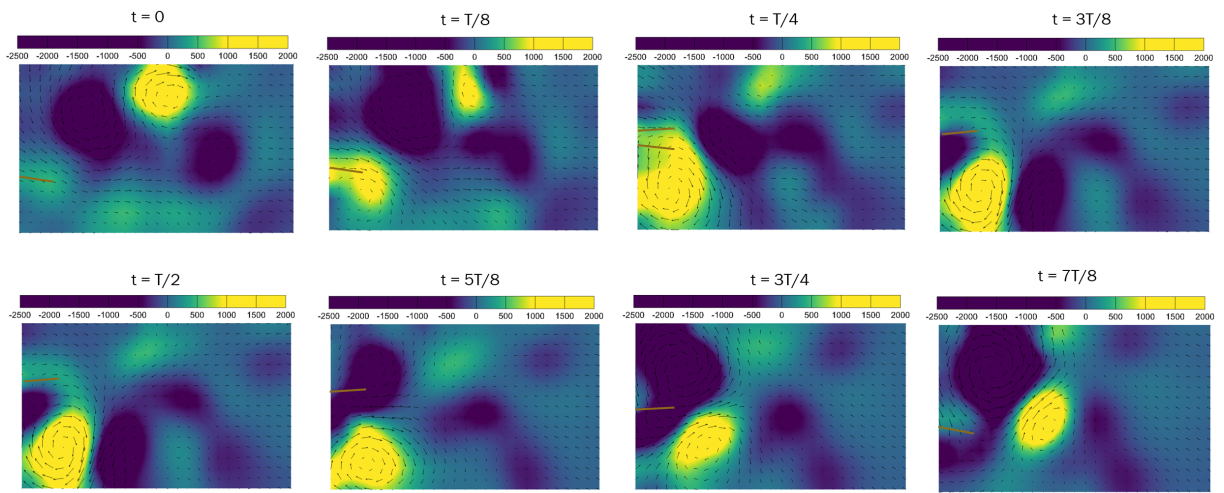


Figure A.3: Time sequence of vortex ($1/s$) formation and evolution in the propagating regime at $Re = 177.2$. Power input = 70V 50Hz.

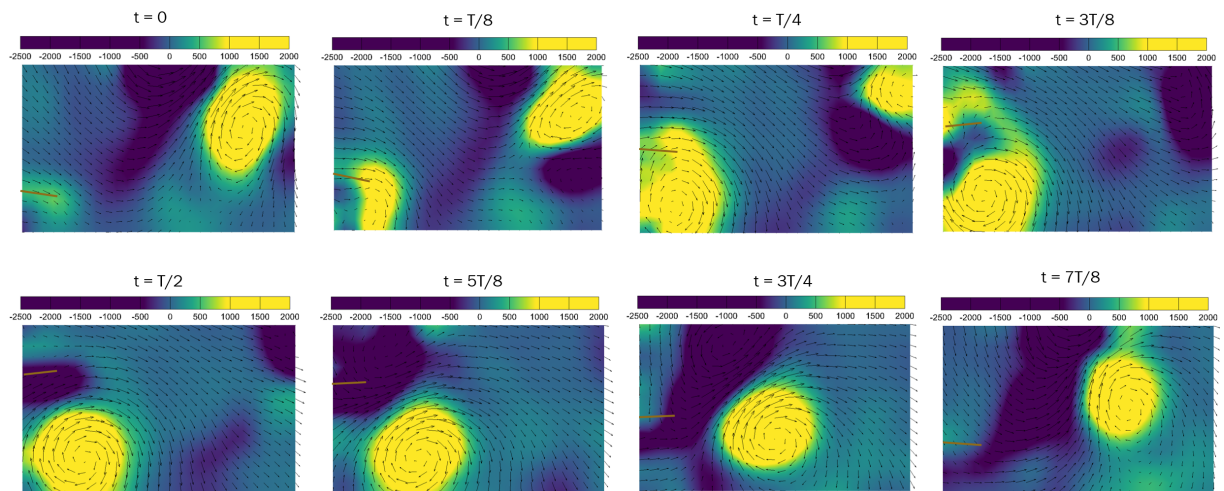


Figure A.4: Time sequence of vortex ($1/s$) formation and evolution in the propagating regime at $Re = 249.1$. Power input = 100V 50Hz.

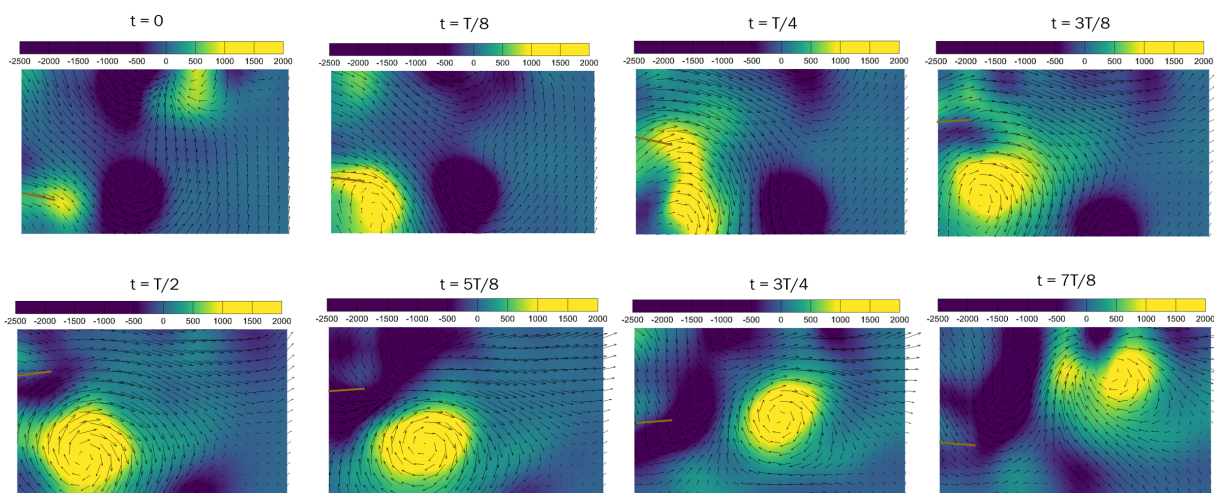


Figure A.5: Time sequence of vortex ($1/s$) formation and evolution in the propagating regime at $Re = 256.9$. Power input = 105V 50Hz.

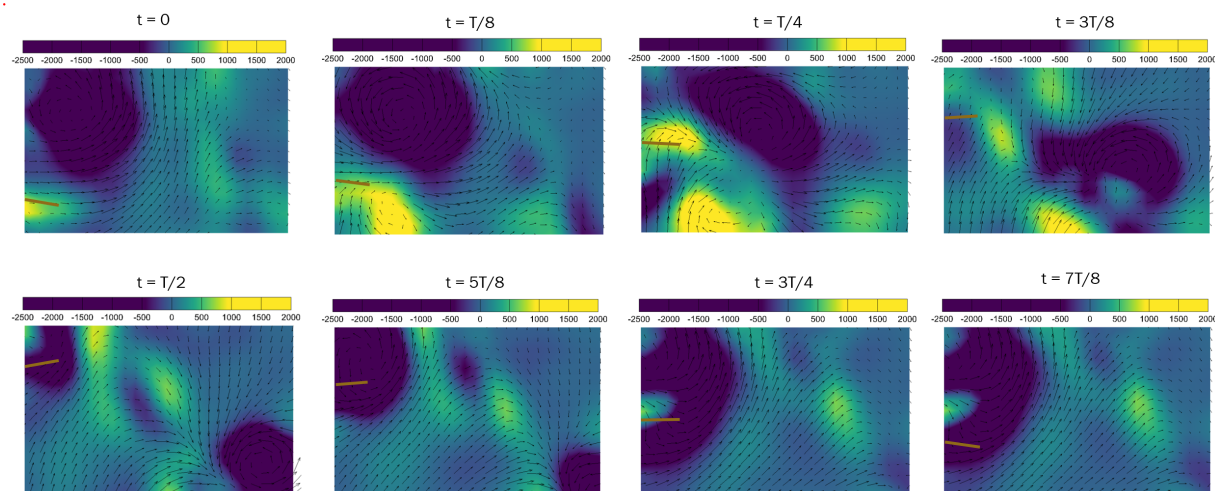


Figure A.6: Time sequence of vortex ($1/s$) formation and evolution in the propagating regime at $Re = 289.9$. Power input = 120V 50Hz.

Appendix B Velocity Magnitude Plots for all Voltages

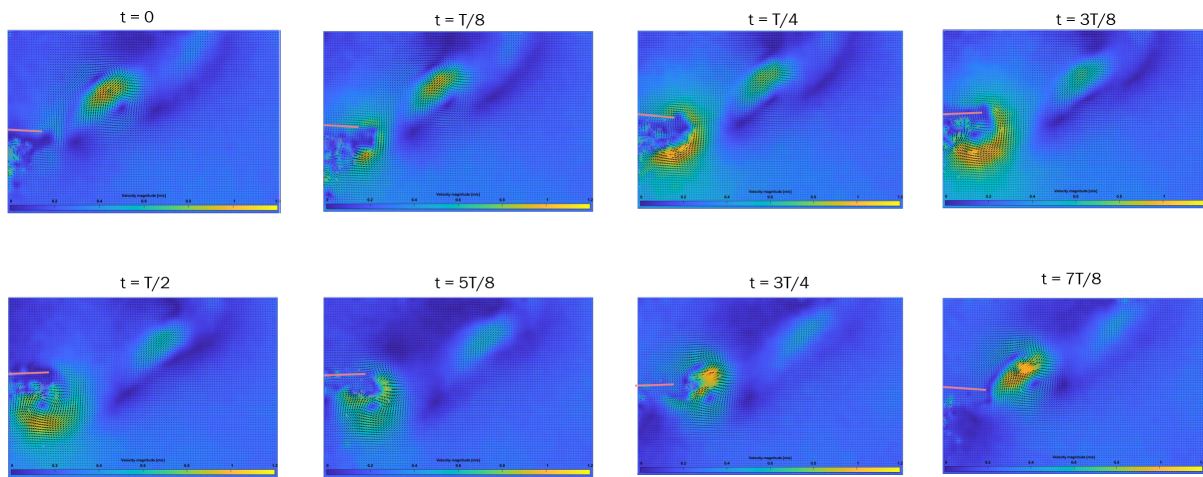


Figure B.1: Time sequence of velocity magnitude evolution in the propagating regime at $Re = 72.4$. Power input = 30V 50Hz.

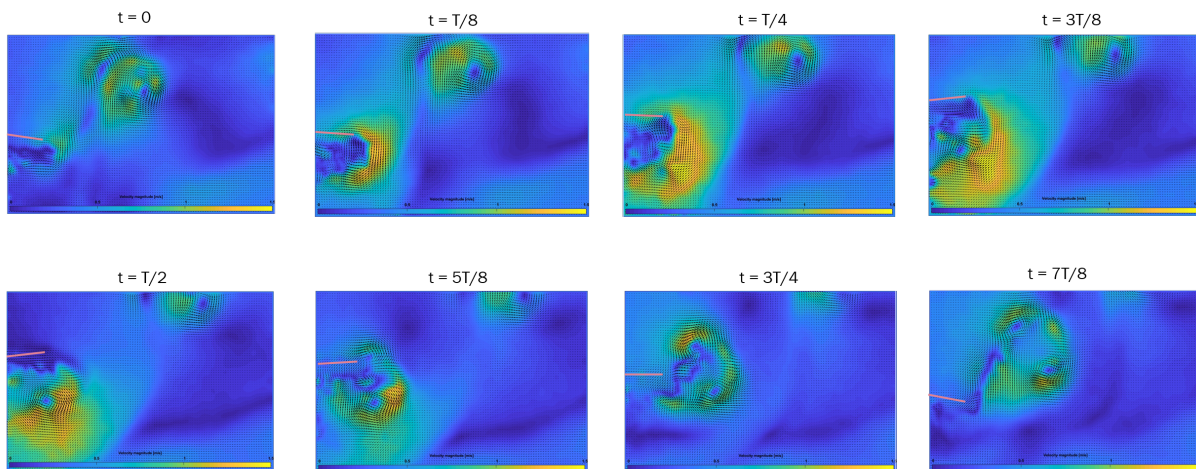


Figure B.2: Time sequence of velocity magnitude evolution in the propagating regime at $Re = 131.8$. Power input = 50V 50Hz

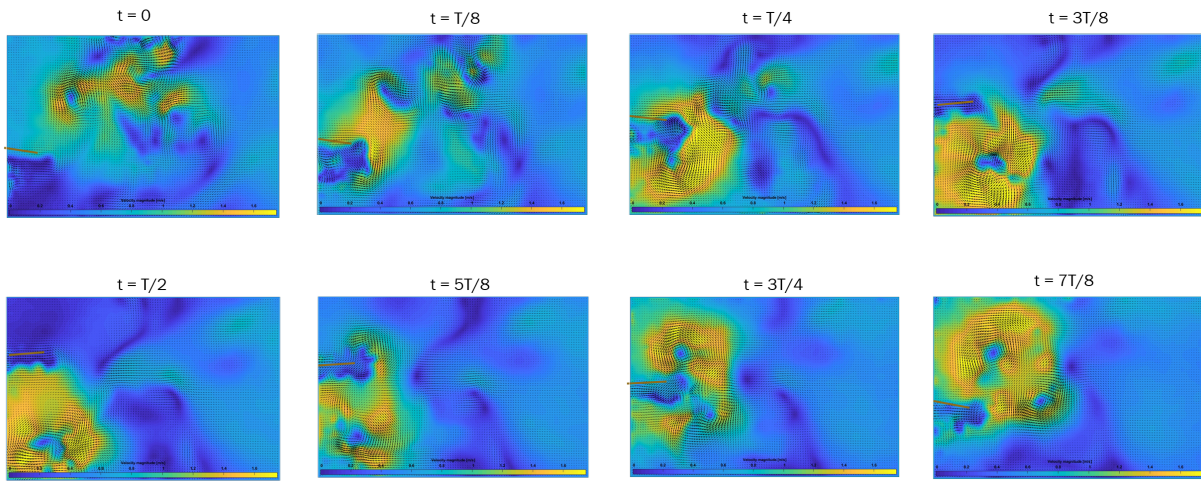


Figure B.3: Time sequence of velocity magnitude evolution in the propagating regime at $Re = 177.2$. Power input = 70V 50Hz.

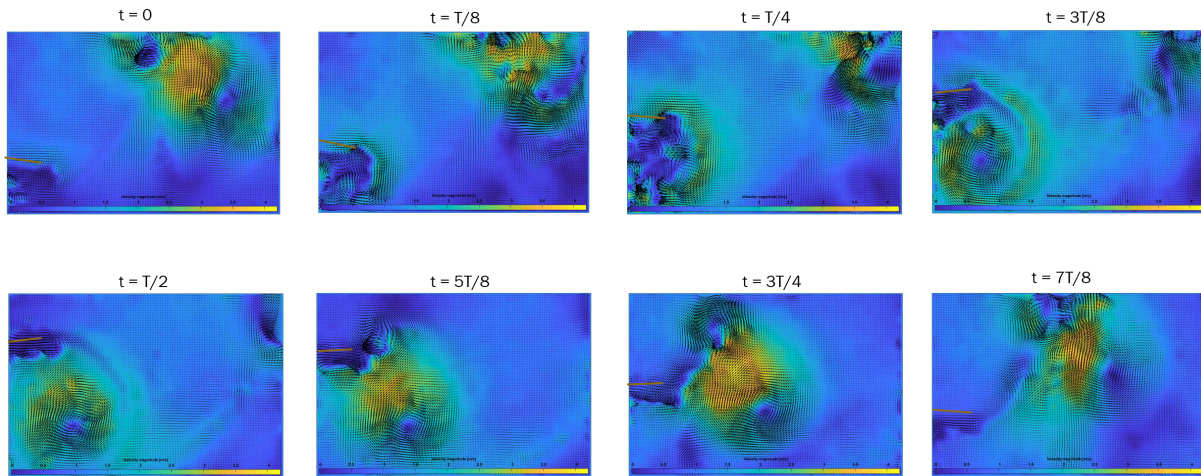


Figure B.4: Time sequence of velocity magnitude formation in the propagating regime at $Re = 249.1$. Power input = 100V 50Hz

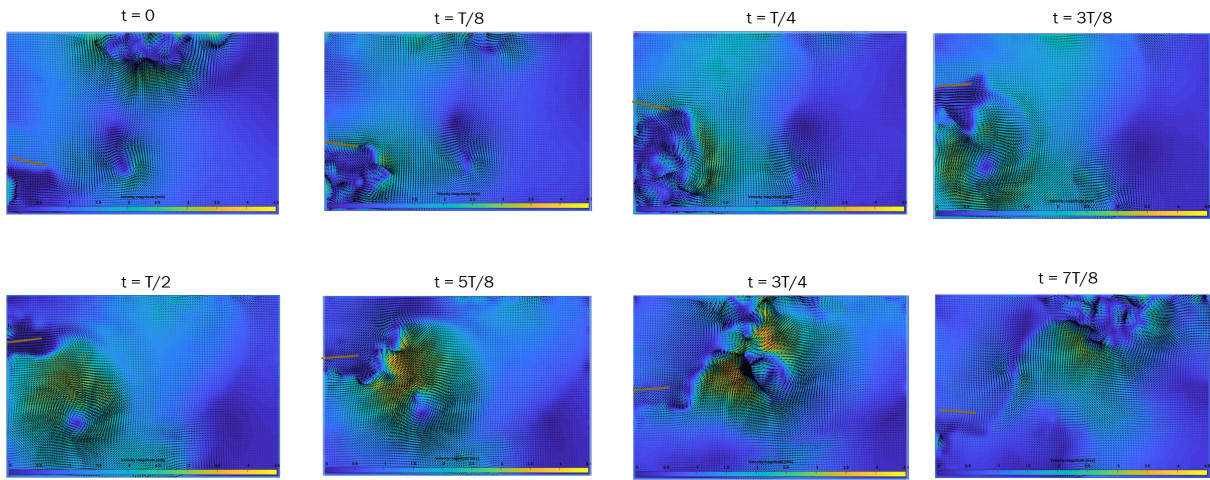


Figure B.5: Time sequence of velocity magnitude evolution in the propagating regime at $Re = 256.9$. Power input = 105V 50Hz.

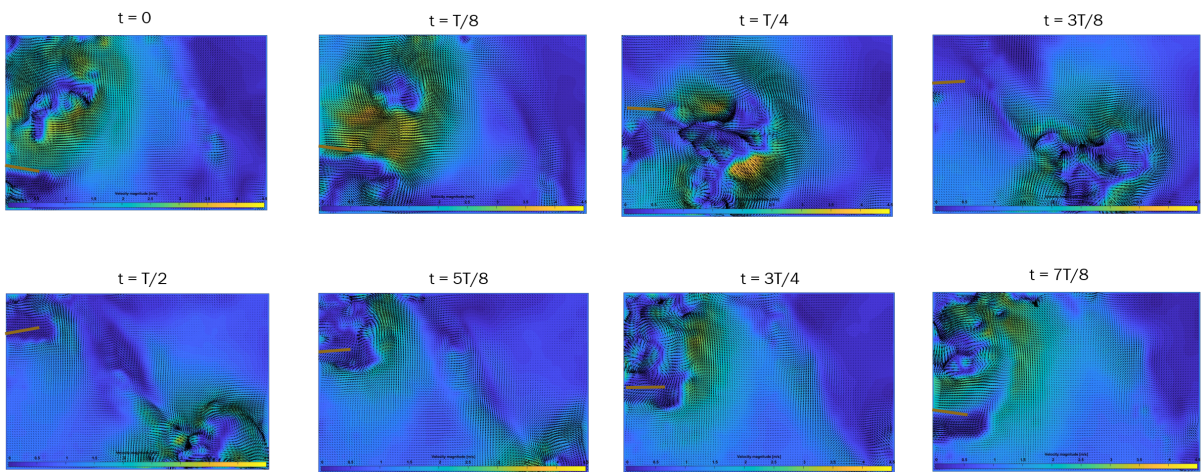


Figure B.6: Time sequence of velocity magnitude evolution in the propagating regime at $Re = 289.9$. Power input = 120V 50Hz.

Appendix C IB2d Manual

C.1 Calculation of Leading and Trailing Edge Positions

Frame speed of 8800 per second is used throughout the experiment to calculate the relationship between image frame number and normalized time $t = T/N$. Pixel locations of leading and

Table 5: Frame numbers for normalized time for leading edge.

V t/T	F=0	F = T/16	F=T/8	F=3/16	F=T/4	F = 5/16	F=3T/8	F = 7/16	F=T/2	F = 9/16	F=5T/8	F = 11/16	F=3T/4	F = 13/16	F=7T/8	F = 15/16	F= T
30V	60	70	81	91	102	112	123	133	144	155	166	177	189	200	211	222	234
50V	176	187	199	210	222	233	245	256	268	278	288	298	309	319	330	340	351
70V	105	116	127	138	150	161	172	183	195	205	215	225	236	246	257	267	278
100V	9	19	29	39	50	60	71	81	92	104	116	128	140	152	164	176	188
105V	167	178	189	200	211	222	233	244	255	266	277	288	299	310	321	332	344
120V	135	146	158	169	181	192	204	215	227	237	247	257	268	278	288	298	309

trailing edges of the fan are measured with `imtool` on MATLAB. The pixel to real-length-ratio from calibration image is then used to calculate the fan’s amplitude in meters.

Transformed amplitude of leading edge from pixel and frame information is plotted on Figure C.2.

Table 6: Pixel location of the leading edge of the fan.

V t/T	F=0	F = T/16	F=T/8	F=3/16	F=T/4	F = 5/16	F=3T/8	F = 7/16	F=T/2	F = 9/16	F=5T/8	F = 11/16	F=3T/4	F = 13/16	F=7T/8	F = 15/16	F= T
30V	365	355	340	329	307	301	288	278	272	274	284	299	316	329	344	355	366
50V	383	376	359	332	306	277	250	240	235	242	264	285	314	341	365	374	382
70V	407	403	381	348	308	267	236	217	208	216	242	268	306	343	384	392	407
100V	447	436	403	360	301	246	214	185	172	180	213	265	327	385	412	441	446
105V	455	439	399	343	283	226	193	170	164	186	225	276	333	390	415	447	456
120V	475	462	415	354	293	222	180	152	138	162	203	263	331	391	419	457	476

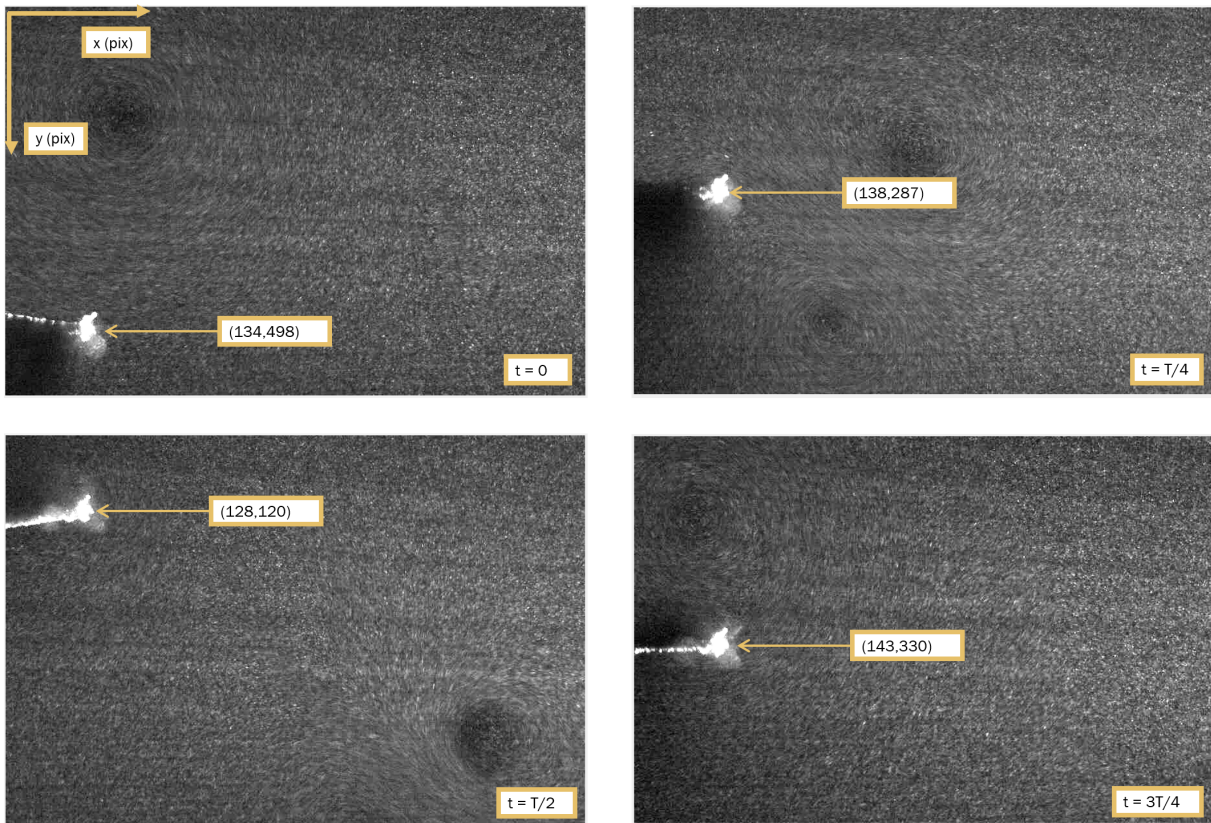


Figure C.1: Measurements of pixel location of the trailing edge. The pixel location measurement is approximated using MATLAB `imtool`.

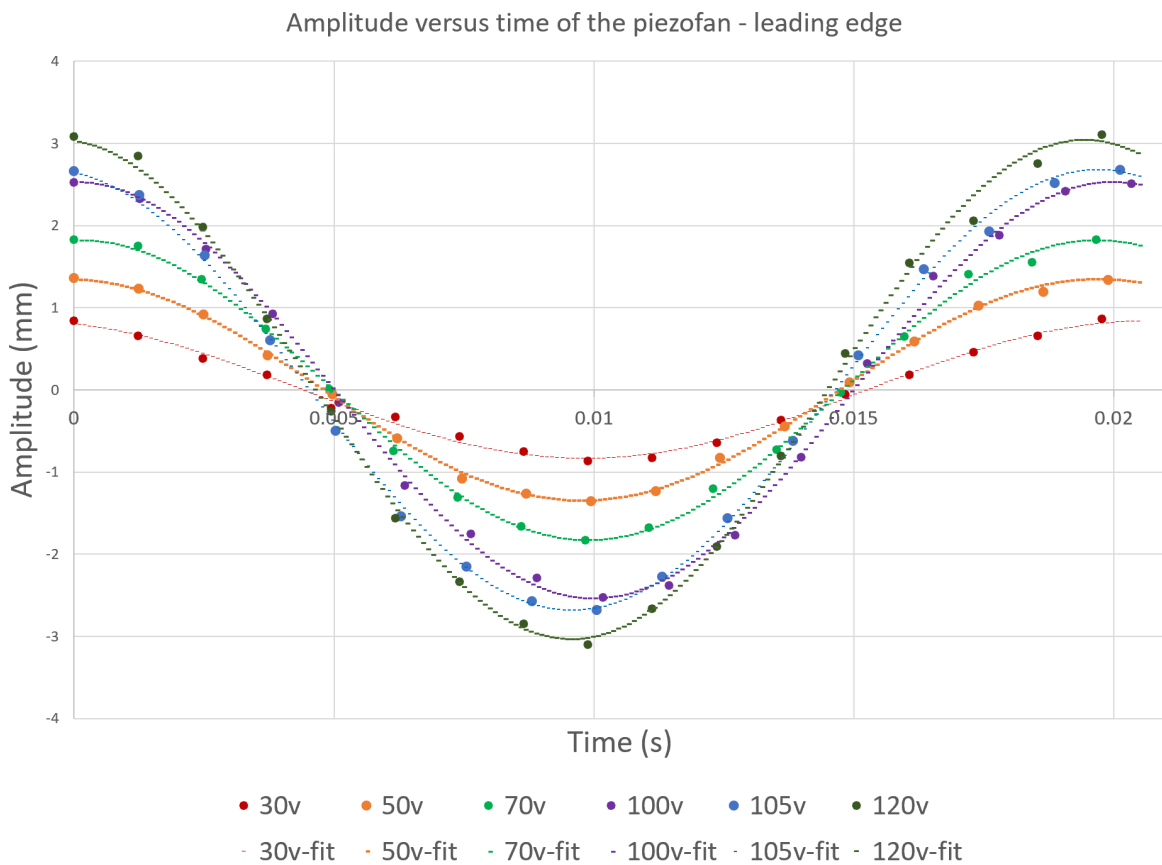


Figure C.2: Amplitude versus time of the leading edge of the fan.

Table 7: Coefficients of sinusoidal model for trailing edge of the piezofan.

Coeff	30v	50v	70v	100v	105v	120v
a	0.8634e-3	1.571e-3	2.112e-3	2.97e-3	3.063e-3	3.456e-3
b	309.5	312	312.2	302	305.8	312.9
c	1.604	1.624	1.593	1.664	1.75	1.678

Table 8: Coefficients of sinusoidal model for leading edge of the piezofan.

Coeff	30v	50v	70v	100v	105v	120v
a	0.8369e-3	1.348e-3	1.825e-3	2.535e-3	2.681e-3	3.038e-3
b	289.3	316.5	320.8	314.6	310.7	318.6
c	1.869	1.63	1.554	1.579	1.744	1.662

Data plotted on Figure C.2 is then analyzed on MATLAB `cftool` to model sinusoidal equation of fan tips. The sinusoidal function is modeled $A(t) = a\sin(bt + c)$ where a, b, and c are amplitude, frequency, and phase-shift of the oscillation. These coefficients are tabulated on Tables 8 and 7.

IB2d is a Python and MATLAB based software developed by Battista [7] to solve fluid-structure interaction problems. The software models interactions of an elastic system that is submerged in uniform density fluid. This software is tinkered and modified to mimic the fluid-structure interaction of a vibrating piezoelectric fan. The baseline software can be found on GitHub under the username `github.com/nickbattista/ib2d`. Battista designed the software in such way that researchers with a different spectrum of programming skills can understand and modify the codes to solve appropriate FSI problems. The black-box folder `../matlIB2d/IBM_Blackbox` includes all methods for resolving interactions between fluid-structures problems. In these codes, the Navier-Stokes equations for updating the fluid velocities throughout the IB2d are solved using vectorized functions. The user shouldn't need to modify the mechanics (in `IBM_Blackbox`) underlying the immersed boundary method unless they want to make additions to the algorithm, e.g. further fiber implementing fiber models, and so forth [7].

Located in the folder where IBM simulation is actually run, lets discuss the individual files: `input2d` file in the testing folder contains fluid parameter values, temporal information, Eulerian grid parameters of the control volume, structural model information of the piezofan, and save commands for post-processing output data.

```

6 % FLUID PARAMETER VALUES %
7 %
8 Fluid_Parameters {
9 mu = 0.0000130993           % Dynamic Viscosity (N*s/m^2)
10 rho = 1.184                % Density (kg/m^2)
11 }
12
13
14 %
15 % TEMPORAL INFORMATION %
16 %
17 Temporal_Information {
18 Tfinal = .250               % Final time of simulation (s)
19 dt = 1e-6                   % Time-step (s)
20 }

```

Figure C.3: Snapshot of `input2d` file. μ , the dynamic viscosity of air on line 9 is calculated to achieve the Reynold's number on experimental data. Re is calculated with Equation 5.

C.2 Target Points

The coordinates for Lagrangian points are transformed through an interpolation function to a new specified location. These Lagrangian points are also called Target points. Each target point is connected to boundary point in the fluid-structure region via a stiff spring with zero resting length. The deformation associated with spring is described in Battista [7].


```

66 % PRINTING INFORMATION
67 %
68 Output_Info {
69 print_dump = 500;           % How often to print (PLOT) to screen
70 save_Vorticity = 1;       % Save Vorticity Scalar Data to .vtk format
71 save_Pressure = 1;        % Save Pressure Scalar Data to .vtk format
72 save_uVec = 1;           % Save u-Vector Data to .vtk format
73 save_uMag = 1;           % Save uMagnitude Scalar Data to .vtk format
74 save_uX = 1;             % Save uX Scalar Data to .vtk format
75 save_uY = 1;             % Save uY Scalar Data to .vtk format
76 save_fMag = 1;           % Save Force Magnitude Scalar Data to .vtk format
77 save_fX = 1;             % Save x-Force Component Scalar Data to .vtk format
78 save_fY = 1;             % Save y-Force Component Scalar Data to .vtk format
79 save_hier = 1;           % Save Scalar Force Data on Lag. Structure to .vtk format
80 plot_Matlab = 0          % Plot in Matlab? (1=YES, 0=NO)
81 plot_LagPts = 0          % Plot Lagrangian Points ONLY in Matlab
82 plot_Velocity = 0        % Plot Lagrangian Points + VELOCITY FIELD in Matlab
83 plot_Vorticity = 0       % Plot Lagrangian Points + VORTICITY colormap in Matlab
84 plot_MagVelocity = 0     % Plot Lagrangian Points + MAGNITUDE OF VELOCITY colormap in Matlab
85 plot_Pressure = 0        % Plot Lagrangian Points + PRESSURE colormap in Matlab
86 }
87
88
89 %
90 % LAGRANGIAN STRUCTURE NAME %
91 %
92 Lag_Name {
93 string_name = "fan"       % String name for simulation
94 }

```

Figure C.4: Snapshot of input2d file. Toggling save_PARM saves and unsaves the signal to .vtk format.

```

32 function Piezo_Fan()
33 % Grid Parameters (MAKE SURE MATCHES IN input2d !!!)
34 %
35 Nx = 64;          % # of Eulerian Grid Pts. in x-Direction (MUST BE EVEN!!!)
36 Ny = 64;          % # of Eulerian Grid Pts. in y-Direction (MUST BE EVEN!!!)
37 Lx = 0.254;       % Length of Eulerian Grid in x-Direction
38 Ly = 0.254;       % Length of Eulerian Grid in y-Direction
39 % Immersed Structure Geometric / Dynamic Parameters %
40 ds = Lx/(2*Nx);  % Lagrangian Spacing
41 struct_name = 'fan'; % Name for .vertex, .spring, etc files.
42 % Call function to construct geometry
43 [xLag,yLag] = give_Me_Immersed_Boundary_Geometry(Lx,ds);
44 % Plot Geometry to test
45 plot(xLag,yLag,'r-'); hold on;
46 plot(xLag,yLag,'*'); hold on;
47 xlabel('x'); ylabel('y');
48 axis([0 Lx 0 Ly]);
49 % Prints .vertex file!
50 print_Lagrangian_Vertices(xLag,yLag,struct_name);
51 % Prints .target file!
52 k_Target = 5.20e8; %pa
53 print_Lagrangian_Target_Pts(xLag,k_Target,struct_name);

```

Figure C.5: Snapshot of `Piezo_Fan_Vertex.m` code. `Piezo_Fan()` places the vertex file of piezofan in the simulation environment.

`main2d.m` is the main function that gets called to run the code. It itself reads parameters from the `input2d` file and passes to `IBM_Blackbox` to drive the simulation.

```

160  %%%%%%%%%%%%%%%%%%%%%%%%%%%%%%%%%%%%%%%%%%%%%%%%%%%%%%%%%%%%%%%%%%%%%%%%%
161  %
162  % FUNCTION: creates the Lagrangian structure geometry
163  %
164  %%%%%%%%%%%%%%%%%%%%%%%%%%%%%%%%%%%%%%%%%%%%%%%%%%%%%%%%%%%%%%%%%%%%%%%%%
165
166  function [xLag,yLag] = give_Me_Immersed_Boundary_Geometry(L,ds)
167  % The immersed structure is a horizontal line
168  Lw = L/15;
169  % Make line geometry of the fan
170  xLag = 0.02:ds:(Lw+0.02);
171  yLag = ones(1,length(xLag))*0.130025;

```

Figure C.6: Snapshot of Piezo_Fan_Vertex.m code. give_Me_Immersed_Boundary_Geometry() places Lagrangian points of the fan on immersed boundary. Line 171 provides the y-coordinate matrix of each Lagrangian point at $t = 0s$.

```

33 function targets = update_Target_Point_Positions(dt,current_time,targets)
34 %length of simulation environment/eularian grid in x-direction
35 Lx = 0.254; % (m)
36 Nx = 64; % number of nodes in x-direction
37 ds = Lx/(2*Nx); %
38 Lw = Lx/15;
39
40 struct_name = 'test_updated_pts';
41 IDs = targets(:,1); % Stores Lag-Pt IDs in col vector
42 xPts = (0.02:ds:(Lw+0.02))';
43 yPts= (ones(1,length(xPts))*Lx/2)';
44 xtemp = xPts;
45
46 y_dis = 3.038/1000*sin(318.6*current_time+1.662)+0.254/2; %leading edge height
47 omega_x = asind((3.456/1000*sin(318.6*current_time))/Lw); % rotational angle (degree)
48
49 %
50 % rotation of wing up and down
51 %
52 yPts = yPts-yDis;
53 xPts = xtemp;
54
55 if (omega_x>=0)
56 rot_mat = @(omega_x) [cos(omega_x) -sin(omega_x); sin(omega_x) cos(omega_x)];
57 else
58 rot_mat = @(omega_x) [cos(omega_x) sin(omega_x); sin(omega_x) -cos(omega_x)];
59 end
60 %calculate the rotation matrix in radians
61 %rotate the x and y points to mimic flapping wing
62 mat =rot_mat(deg2rad(omega_x));
63 f_rot = mat*[xPts';yPts'];
64 f_rot(2,:)=f_rot(2,:)+ y_dis;
65 targets(:,2) = f_rot(1,:)';
66 targets(:,3) = f_rot(2,:)';

```

Figure C.7: Snapshot of `update_Target_Point_Positions.m` code. Line 46 and 47 define the heights of leading edge and angle of the trailing edge. These sinusoidal equations are retrieved using `cftool` on experimental data.